# An engineered human cardiac tissue model reveals contributions of systemic lupus erythematosus autoantibodies to myocardial injury

Sharon Fleischer[1,11], Trevor R. Nash [1,11], Manuel A. Tamargo[1], Roberta I. Lock[1], Gabriela Venturini[2], Margaretha Morsink[1], Pamela L. Graney [1], Vanessa Li[1], Morgan J. Lamberti[1], Martin Liberman[1], Youngbin Kim [1], Daniel N. Tavakol[1], Richard Z. Zhuang[1], Jaron Whitehead[1], Richard A. Friedman[3,4], Rajesh K. Soni[5], Jonathan G. Seidman [2], Christine E. Seidman[2,6,7], Laura Geraldino-Pardilla[8], Robert Winchester[8,9] & Gordana Vunjak-Novakovic [1,8,10] ✉

Systemic lupus erythematosus (SLE) is a heterogenous autoimmune disease that affects multiple organs, including the heart. The mechanisms of myocardial injury in SLE remain poorly understood. In this study, we engineered human cardiac tissues and cultured them with IgG from patients with SLE, with and without myocardial involvement. IgG from patients with elevated myocardial inflammation exhibited increased binding to apoptotic cells within cardiac tissues subjected to stress, whereas IgG from patients with systolic dysfunction exhibited enhanced binding to the surface of live cardiomyocytes. Functional assays and RNA sequencing revealed that, in the absence of immune cells, IgG from patients with systolic dysfunction altered cellular composition, respiration and calcium handling. Phage immunoprecipitation sequencing (PhIP-seq) confirmed distinctive IgG profiles between patient subgroups. Coupling IgG profiling with cell surfaceome analysis identified four potential pathogenic autoantibodies that may directly affect the myocardium. Overall, these insights may improve patient risk stratification and inform the development of new therapeutic strategies.

Myocardial involvement occurs in 25–50% of patients with systemic lupus erythematosus (SLE), including those without symptoms, and can result in myocardial inflammation with ventricular dysfunction, progression to heart failure and high rates of mortality[1–7]. Organ damage in SLE is presumed to be driven by both T cells and specific autoantibody populations that react with the host tissue, form immune complexes and drive inflammation[8–10]. In the heart, the identity and mechanisms by which autoantibodies contribute to myocardial injury remain elusive. Growing evidence suggests that autoantibodies can directly mediate myocardial injury. Congenital heart block in neonates exposed to maternal SLE autoantibodies through passive transfer across the placenta provides evidence that injury can occur through the direct effects of autoantibody binding[11–15]. This paradigm is further supported by evidence in other autoimmune conditions in which autoantibodies binding to cardiac surface proteins, including ion channels and β-adrenergic receptors, impair calcium handling and action potential propagation, increase reactive oxygen species (ROS), activate apoptosis and cause heart failure and arrhythmias[16–24]. In addition, multiple
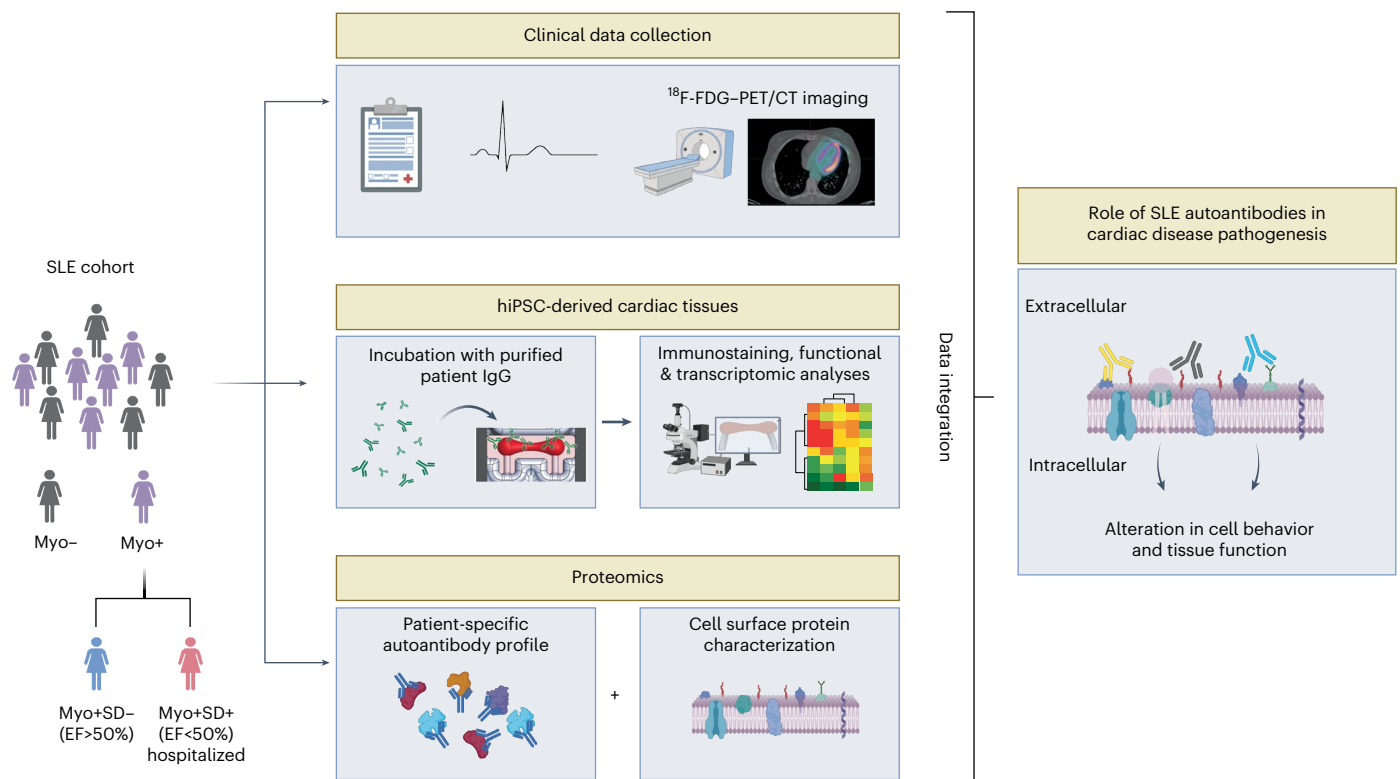
**Fig. 1 | Overview of the experimental design.** Figure was created using BioRender.

studies have reported direct contributions of SLE autoantibodies to alterations in brain function by directly modulating cellular processes in neurons[25,26]. Taken together, these studies further suggest that, in addition to complement-mediated and immune cell-mediated myocardial injury, autoantibodies may directly lead to cardiac dysfunction via independent mechanisms. Additionally, the absence of reports identifying a specific autoantibody target linked to a particular SLE disease phenotype, either in general or specifically related to myocardial involvement, suggests that multiple SLE autoantibodies act in concert to induce injury. This underscores the complex nature of the disease and the need to investigate the effect of the full repertoire of patient-specific autoantibodies on cardiac tissue function to identify autoantibodies that together lead to myocardial injury in SLE.

Cardiomyocytes derived from human induced pluripotent stem cells (hiPSC-CMs) represent a promising approach for modeling human cardiac pathophysiology in vitro. We previously reported improved maturation of hiPSC-CMs within engineered human cardiac tissues by an electromechanical stimulation regimen that gradually increases the stimulation frequency from 2 Hz to 6 Hz (ref. 27). This 'intensity training' regimen subjects tissues to stress while also promoting the development of features similar to those of a more mature human myocardium, including metabolism, ultrastructure and electrophysiology[27,28].

Notably, cellular stress in SLE has been associated with the redistribution and clustering of intracellular autoantigens to apoptotic blebs on the surface of the plasma membrane[29–31]. Antigenic fragments created in these blebs, often in relation to ROS generation, evoke autoimmune inflammatory responses in some patients with SLE, unlike those without such cellular stress[29,30]. Therefore, we hypothesized that stress in the adult human heart could lead to differential autoantibody binding patterns and modulate autoantibody-mediated myocardial injury. To test this hypothesis, we used the intensity training regimen to simulate stress-induced cellular processes, including antigen redistribution, and thereby capture potential additional aspects of disease pathogenesis.

We cultured engineered human cardiac tissue models with serum-derived, purified IgG fractions from individual patients with SLE to capture the full autoantibody repertoire of each patient and the patient-specific effects of purified IgG on cardiac tissue function. Patients with SLE with and without clinical evidence of myocardial inflammation (Myo+ and Myo− patients, respectively) were delineated based on $^{18}$F-fluorodeoxyglucose ($^{18}$F-FDG) uptake in positron emission tomography/computed tomography imaging ($^{18}$F-FDG–PET/CT). The Myo+ group included patients with SLE with new-onset systolic dysfunction (SD), defined as left ventricular ejection fraction (EF) less than 50% at the time of serum collection (denoted Myo+SD+), and patients with preserved EF (EF > 50%, denoted Myo+SD−). IgG binding to cardiac tissues was quantified, and the impact of binding on tissue function and molecular and transcriptional profiles was assessed. Using phage immunoprecipitation sequencing (PhIP-seq), we characterized patient-specific autoantibody targets, and, using liquid chromatography with tandem mass spectrometry (LC–MS/MS), we profiled cell surface accessible antigens on cardiomyocytes and cardiac fibroblasts to inform the identification of pathogenic autoantibody candidates (Fig. 1).

## Results

### SLE cohorts

Samples were obtained from patients enrolled in two different SLE cohorts: one pre-existing cohort of patients without cardiac symptoms who were receiving treatment in the outpatient setting and one prospective cohort of patients who were hospitalized for active cardiac disease. Patients with SLE met the 1997 American College of Rheumatology (ACR) classification criteria[32]. Clinical studies of $^{18}$F-FDG uptake were conducted for all patients, both hospitalized and non-hospitalized, to determine the presence of myocardial inflammation. All $^{18}$F-FDG–PET/CT scans were evaluated qualitatively for the presence or absence of enhanced myocardial $^{18}$F-FDG uptake, and, for a subset of patients, levels of $^{18}$F-FDG uptake were quantified by standardized uptake values

(SUVs)[33] (Methods). Patients with SLE were divided into two primary groups based on myocardial ^{18}F-FDG uptake: (1) Myo− patients were without evidence of myocardial inflammation (SUVmax < 1.5; $n$ = 3); (2) Myo+ patients had evidence of myocardial inflammation (SUVmax ≥ 1.5; $n$ = 8). At the time of ^{18}F-FDG–PET/CT, serum samples were collected, and echocardiograms were obtained to distinguish between Myo+ patients with SD (Myo+SD+, $n$ = 4, with EF < 50%) and Myo+ patients with preserved systolic function (Myo+SD−, $n$ = 4, EF ≥ 50%). No patients in either group had elevated serum troponin. Notably, at the time of the study, all Myo+SD+ patients had recent-onset SD that had not been documented previously in their medical records. Additionally, no patients in either group had histories of ischemic heart disease, and no significant differences were observed in cardiovascular risk factors between groups. Detailed clinical data are summarized in Table 1.

## Engineering human cardiac tissues with advanced properties

Cardiac tissues were engineered by resuspending hiPSC-CMs and primary human cardiac fibroblasts at a 3:1 ratio in fibrin hydrogels, stretched between two flexible pillars and electromechanically stimulated using our previously published milliPillar platform[28]. Electromechanical stimulation frequency was increased from 2 Hz to 6 Hz over 2 weeks (intensity training regimen), followed by an additional week of stimulation at 2 Hz, as previously described[27]. To further enhance tissue performance, tissues were cultured in maturation medium (MM) previously reported to shift cardiomyocyte metabolism from glycolysis toward fatty acid oxidation, increase mitochondrial content and optimize cardiomyocyte function[34] (detailed in Methods; Fig. 2a, top panel). Tissues exhibited enhanced compaction, α-actinin striations and calcium handling as compared to those cultured in standard medium (Extended Data Fig. 1a–c). No effect on tissue contractility was observed (Extended Data Fig. 1d). Tissue stimulation at 6 Hz resulted in significantly increased release of lactate dehydrogenase (LDH), indicative of cellular stress (Extended Data Fig. 1e).

## IgG binding to stressed cardiac tissues

IgG fractions were purified and quantified from each patient's serum sample. At day 14 of cardiac tissue culture, IgG fractions from individual patients were added to the culture media, and tissues were cultured for 14 additional days in which tissues were subjected to stress as part of the intensity training regimen (Fig. 2a, bottom panel). To evaluate the extent of patient IgG binding to tissue antigens accessible to them during culture, the tissues were fixed at day 28 and subsequently stained with secondary anti-human IgG. Patient IgG binding levels were measured as mean fluorescence intensity (MFI). Tissues cultured with IgG from all Myo− patients exhibited low MFI levels. Within the Myo+ group, tissues cultured with IgG from a subset of patients exhibited low MFI levels, whereas substantially higher MFI levels were observed for a different subset of patients who had elevated levels of myocardial inflammation (Fig. 2b and Extended Data Fig. 2a). MFI levels of tissues cultured with IgG from an additional Myo+ patient with high levels of myocardial ^{18}F-FDG uptake (SUVmax = 12.4) confirmed this trend (Extended Data Table 1 and Extended Data Fig. 2b). Linear regression analysis (inclusive of all patients with ^{18}F-FDG uptake quantification, $n$ = 9) revealed a significant positive correlation between MFI and levels of myocardial inflammation measured by SUV ($r^2$ = 0.88, $P$ = 0.0002; Fig. 2c). MFI correlated more strongly with myocardial inflammation than did any clinical metric of myocardial health or SLE severity (Extended Data Fig. 3a).

Further studies comparing the extent of IgG binding to stressed and non-stressed hiPSC-CMs revealed that stress led to a significant increase in IgG binding across all patients. Notably, a significant difference in IgG binding levels between patients with SLE with low myocardial inflammation levels (SUVmax < 10) and elevated myocardial inflammation (SUVmax > 10) was observed only in the stressed hiPSC-CMs, further highlighting the contribution of stress to

differential IgG binding patterns among patients with SLE (Extended Data Fig. 3b). IgG binding to healthy left ventricle (LV) human tissue samples revealed similar patterns of IgG binding to non-stressed cardiac tissues, with no significant difference in MFI between patients with high and low levels of myocardial inflammation (Extended Data Fig. 3c).

To further probe the cellular targets of patient IgG, tissues were co-stained with secondary anti-human IgG and α-actinin to evaluate cardiomyocyte integrity and IgG localization. The extent of IgG binding within the stressed tissues varied from cell to cell (Fig. 2d). A subset of cells with patient IgG staining were cardiomyocytes with disrupted α-actinin striations and condensed nuclei, with IgG binding primarily to the nuclei, indicating late cell apoptosis with loss of cell membrane integrity that allowed IgG penetration (Fig. 2d). Additionally, we identified another subset of cells with high levels of localized IgG binding to presumptive apoptotic blebs on surfaces of cardiomyocytes with minimal nuclear condensation (Fig. 2e). Flow cytometric analysis revealed significantly higher IgG binding levels to the apoptotic cell population (Apo+) when compared to live, non-apoptotic cells (Apo−) for IgG from patients with elevated myocardial inflammation. Furthermore, for IgG from two of these patients with elevated myocardial inflammation, no significant differences were observed in IgG binding to stressed Apo− cells and non-stressed Apo− cells, and, for IgG from another patient with elevated myocardial inflammation, stress reduced IgG binding levels to Apo− cells (Extended Data Fig. 3d–g). These data suggest that for IgG from patients with SLE with elevated myocardial inflammation, the heightened IgG binding to cardiac tissues is primarily attributed to increased binding to stress-induced apoptotic cells.

## IgG binding to the surface of live cardiomyocytes

As previous studies have reported that autoantibodies bound to plasma membrane targets can directly exert biological effects[11,16–20], we investigated the patterns of IgG binding to the surfaces of the live cardiomyocyte populations. Live hiPSC-CMs were incubated with patient IgG fractions, followed by incubation with secondary anti-human IgG, and then sorted using flow cytometry to exclude dead and apoptotic cells. A significant correlation between IgG binding levels (MFI) to live hiPSC-CMs and EF was observed ($r^2$ = 0.54, $P$ = 0.0095; Fig. 2f). Consistently, IgG from Myo+SD+ patients with SLE exhibited significantly higher binding levels to the surface of live hiPSC-CMs compared to IgG binding from all other patient groups and healthy controls (Fig. 2g and Extended Data Fig. 3h).

## Myo+SD+ IgGs alter cardiac tissue composition and function

We next sought to investigate whether direct IgG binding to the surface of hiPSC-CMs exerted functional effects on cardiac tissues. After 14 days of tissue incubation with IgG from individual patients with SLE or healthy controls (Fig. 3a), tissues were studied by immunofluorescence staining for α-actinin and vimentin. A higher level of vimentin staining, indicative of fibroblast content, was observed in cardiac tissues cultured with IgG from Myo+SD+ patients. To confirm this effect, we treated fibroblasts in monolayers with IgG from Myo+SD+ patients and observed a significant increase in Ki-67-positive cells, indicating increased fibroblast proliferation (Fig. 3c).

As autoantibodies can alter cardiomyocyte calcium homeostasis and activate β-adrenergic stimulation[17,20,22,23], we assessed cardiac tissue calcium handling and contractile function using non-invasive data acquisition and analysis modalities (Extended Data Fig. 4a–d). In comparison to baseline, before IgG addition, calcium transient decay constant (tau, τ) and transient amplitude width (full width at half maximum (FWHM)) after 7 days were significantly higher in tissues cultured with IgG from Myo+SD+ patients compared to all other groups, indicating impaired calcium handling (Fig. 3d–f). These results were further supported by dose-dependent increases in tau and FWHM in hiPSC-CM monolayers cultured with increasing concentrations of IgG from Myo+SD+ patients (Extended Data Fig. 5a,b).

**Table 1 | Patient cohort clinical characteristics**

| Group | Myocardial inflammation (−) | | | Myocardial inflammation (+) | | | | | | | |
|---|---|---|---|---|---|---|---|---|---|---|---|
| Subgroup | N/A | | | Systolic dysfunction (−) | | | | Systolic dysfunction (+) | | | |
| Patient descriptor | Myo−_1 | Myo−_2 | Myo−_3 | Myo+SD−_1 | Myo+SD−_2 | Myo+SD−_3 | Myo+SD−_4 | Myo+SD+_1 | Myo+SD+_2 | Myo+SD+_3 | Myo+SD+_4 |
| Study ID | 1275 | 523 | 2526 | 472 | 594 | 558 | 666 | 7700 | 5481 | 5,708 | 5076 |
| Age (years) | 30 | 45 | 26 | 37 | 38 | 34 | 25 | 23 | 43 | 46 | 39 |
| Sex | Female | Female | Female | Male | Female | Female | Female | Female | Female | Female | Female |
| Level of care | Outpatient | Outpatient | Outpatient | Outpatient | Outpatient | Outpatient | Outpatient | Inpatient | Inpatient | Inpatient | Inpatient |
| Disease duration (years) | 10 | 34 | 5 | 8 | 4 | 12 | 8 | 5 | 7 | 22 | 28 |
| FDG-uptake (SUVmax) | 1.2 | 1.3 | 1.1 | 10.7 | 1.9 | 2.4 | 1.8 | 14.8 | Positive | Positive | Positive |
| EF (%) | 55–60 | 60–65 | 62 | 55 | 60–65 | 60–65 | 58 | 35 | 47 | 45–50 | 10–15 |
| QTc (ms) | 423 | 428 | 467 | 416 | 438 | 437 | 411 | 493 | 486 | 438 | 488 |
| Troponin (ng ml$^{-1}$) | <0.01 | <0.01 | <0.01 | <0.01 | <0.01 | <0.01 | <0.01 | <0.01 | <0.01 | <0.01 | <0.01 |
| ACR criteria | 4 | 10 | 7 | 10 | 3 | 7 | 9 | 11 | 11 | 11 | 5 |
| SLEDAI | 4 | 0 | 4 | 2 | 4 | 5 | 5 | 18 | 10 | 0 | 0 |
| ESR (mm h$^{-1}$) | 17 | 27 | 44 | 28 | 22 | 45 | 5 | 57 | 79 | 55 | 60 |
| CRP (mg l$^{-1}$) | 3.2 | 1.41 | 5.37 | 0.25 | 2 | 0.84 | 0.3 | 12.4 | 5.88 | 1.65 | 67.27 |
| C3 (mg dl$^{-1}$) | 126 | 61 | 125 | 92 | 133 | 121 | 77 | 144 | 119 | 83 | 163 |
| C4 (mg dl$^{-1}$) | 28 | 5 | 36 | 30 | 33 | 24 | 8 | 26 | 22 | 20 | 23 |
| Anti-dsDNA antibody (IU) | <6 | 245.5 | 47.9 | 121.2 | 14.9 | 7.6 | 13.5 | 52.2 | 62.1 | 24 | 7.4 |
| SSA antibody (AI) | 0.9 | <0.2 | <0.2 | >8 | 3.7 | >8 | <0.2 | >8 | <0.2 | <0.2 | <0.2 |
| SSB antibody (AI) | <0.2 | <0.2 | <0.2 | >8 | <0.2 | 0.5 | <0.2 | >8 | <0.2 | <0.2 | <0.2 |
| Smith antibody (AI) | <0.2 | 0.9 | <0.2 | 0.6 | <0.2 | <0.2 | <0.2 | 7.3 | 0.3 | <0.2 | <0.2 |
| B2GP IgG (SGU) | 0 | 0 | 0 | 0 | 0 | 0 | 1 | 1 | 2 | 17 | 13 |
| B2GP IgM (SMU) | 3 | 1 | 0 | 2 | 2 | 2 | 7 | 2 | 5 | 0 | 34 |
| ACL IgG (GPL) | 5 | 2 | 2 | 0 | 2 | 4 | 2 | 0 | 1 | 18 | 28 |
| ACL IgM (MPL) | 2 | 5 | 0 | 0 | 0 | 3 | 10 | 0 | 5 | 0 | 11 |
| HbA1c (%) | 5 | 4.8 | 4.7 | 5.5 | 4.8 | 4.9 | 4.5 | 5 | 4.5 | 5.8 | |
| Systolic BP (mm Hg) | 108 | 100 | 104 | 98 | 127 | 94 | 120 | 140 | 110 | 145 | 100 |
| Diastolic BP (mm Hg) | 68 | 60 | 60 | 68 | 89 | 60 | 50 | 100 | 70 | 90 | 60 |
| BMI (kg m$^{-2}$) | 23.41 | 22.4 | 27.34 | 21.28 | 29.19 | 23.36 | 20.01 | 27.17 | 29.62 | 28.5 | 36.13 |
| Total cholesterol (mg dl$^{-1}$) | 268 | 182 | 170 | 132 | 151 | 178 | 169 | 275 | 174 | 171 | 172 |
| Triglycerides (mg dl$^{-1}$) | 74 | 64 | 74 | 50 | 65 | 78 | 109 | 77 | 105 | 84 | |
| HDL (mg dl$^{-1}$) | 69 | 46 | | 39 | 55 | 57 | 57 | 67 | 64 | 46 | |
| LDL (mg dl$^{-1}$) | 184 | 123 | | 83 | 83 | 105 | 90 | 193 | 90 | 108 | |

All patients in the cohort fulfilled the ACR classification criteria for SLE. Patients were grouped based on the presence or absence of myocardial inflammation assessed by $^{18}$F-FDG uptake (Myo+ and Myo−, respectively). Patients with SLE with no $^{18}$F-FDG uptake quantification are reported as positive based on qualitative analysis. Myo+ patients were further subgrouped based on SD. All patients with SLE had positive antinuclear antibody titers, and levels of specific antinuclear antibodies (that is, anti-dsDNA, anti-SSA, anti-SSB and anti-Smith) are included here. Levels of specific antiphospholipid antibodies (that is, anti-B2GP and anti-ACL) are included as well. ACL, anticardiolipin; AI, antibody index; B2GP, beta-2-glycoprotein; BMI, body mass index; BP, blood pressure; CRP, C-reactive protein; ESR, erythrocyte sedimentation rate; GPL, IgG phospholipid units; HbA1c, hemoglobin A1c; HDL, high-density lipoprotein; IU, international units; LDL, low-density lipoprotein; MPL, IgM phospholipid units; QTc, corrected QT interval; SGU, standard IgG anti-beta 2 GP1 units; SLEDAI, systemic lupus erythematosus disease activity index; SMU, standard IgM anti-beta 2 GP1 units. Blank values indicate data that were not available from accessible clinical records.
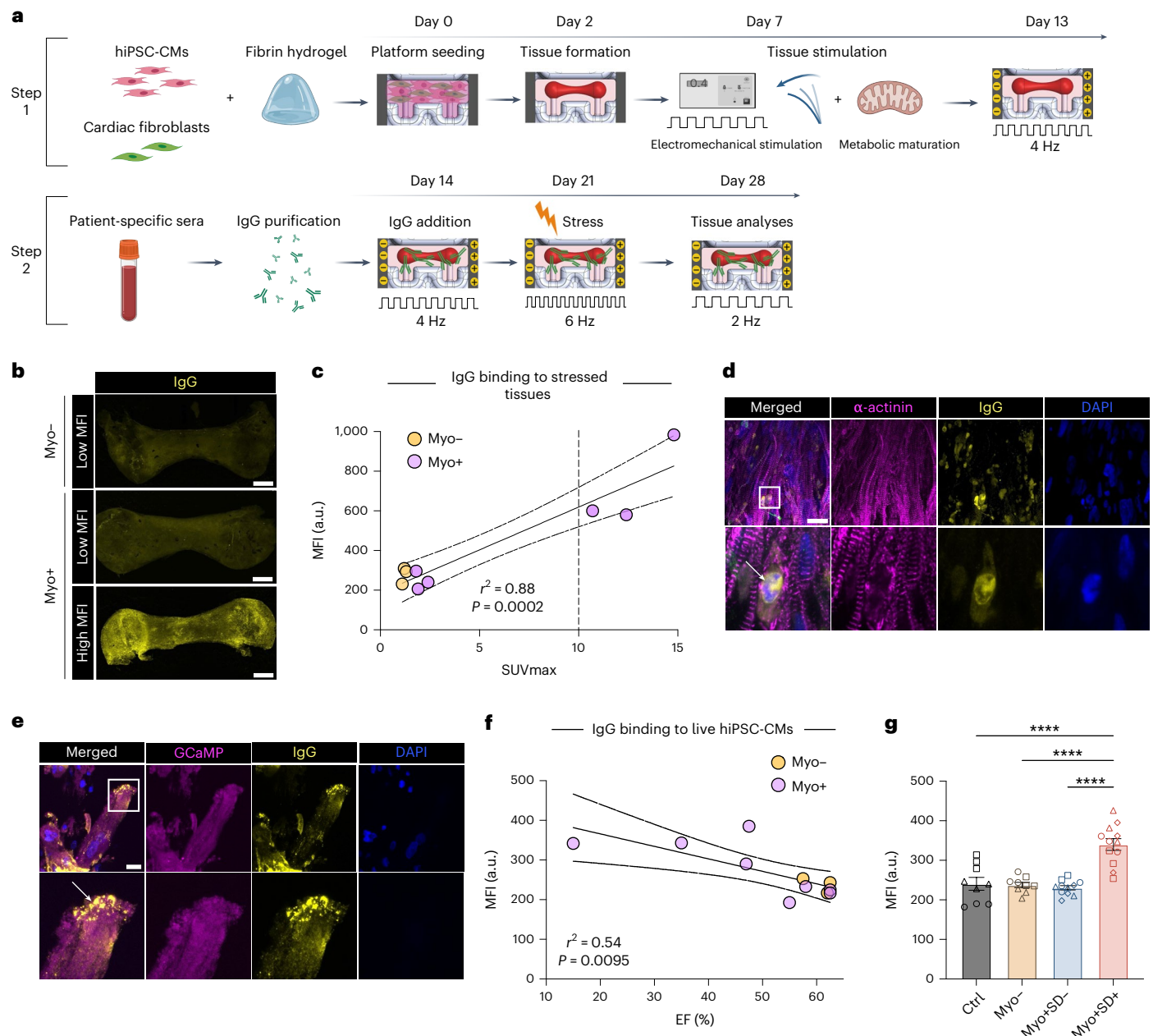
**Fig. 2 | Distinct patient IgG reactivity with engineered cardiac tissues and hiPSC-CMs corresponds with specific clinical outcomes. a**, Overview of tissue formation, stimulation and treatment with purified patient sera-derived IgG. Each tissue was cultured with IgG from one specific patient. **b**, Immunofluorescence staining of human IgG (yellow) derived from patient sera and bound to engineered cardiac tissues (scale bar, 500 μm). **c**, Linear correlation between patient IgG binding levels to engineered cardiac tissues (MFI) and clinical measurements of myocardial inflammation (^{18}F-FDG uptake quantified as SUVs). Each dot represents a patient ($n = 9$), and dots with SUVmax > 10 represent patients with elevated myocardial inflammation. $P$ value and $r^2$ were calculated by two-tailed Pearson's correlation analysis. **d,e**, Immunofluorescence staining of engineered cardiac tissues showing strong sera-derived IgG binding to condensed nuclei (**d**; scale bar, 20 μm; bottom panels are higher magnification of region of interest in top panels; top panel is confocal maximum intensity

projection; bottom panel is single confocal plane) and apoptotic blebs on the cell surface (**e**; scale bar, 20 μm; bottom panels are higher magnification of region of interest in top panels; both panels are single confocal planes). **f**, Linear correlation between patient IgG binding levels to the cell surface of live hiPSC-CMs (MFI) and corresponding patient EF. Each dot represents a patient ($n = 11$). $P$ value and $r^2$ were calculated by two-tailed Pearson's correlation analysis. **g**, Quantification using flow cytometry of patient IgG binding to live hiPSC-CMs based on clinical subgroupings. MFI indicates median fluorescence intensity. Data are represented as mean ± s.e.m. $n = 3$ healthy control patients, $n = 3$ Myo− patients, $n = 4$ Myo+SD− patients and $n = 4$ Myo+SD+ patients ($n = 2$–3 independent replicate wells per patient sample; exact replicate values are included in Supplementary Table 1). Symbol shapes represent different patients within each group; one-way ANOVA with Tukey's test for multiple comparisons; ****$P < 0.0001$. Ctrl, control.

In addition, a dose-dependent decrease in beating frequency was observed in hiPSC-CMs after 24 hours, which was also significantly lower in hiPSC-CMs cultured with IgG from Myo+SD+ patients when compared to hiPSC-CMs cultured with IgG from Myo− and Myo+SD− patients at the highest IgG concentration (Extended Data Fig. 5c).

This trend was also observed in hiPSC-CMs 1 hour after the addition of patient IgG (Extended Data Fig. 5d), suggesting that Myo+SD+ IgG did not act as agonists to β-adrenergic receptors. Finally, no significant differences were observed in cardiac tissue force generation in response to patient IgG.
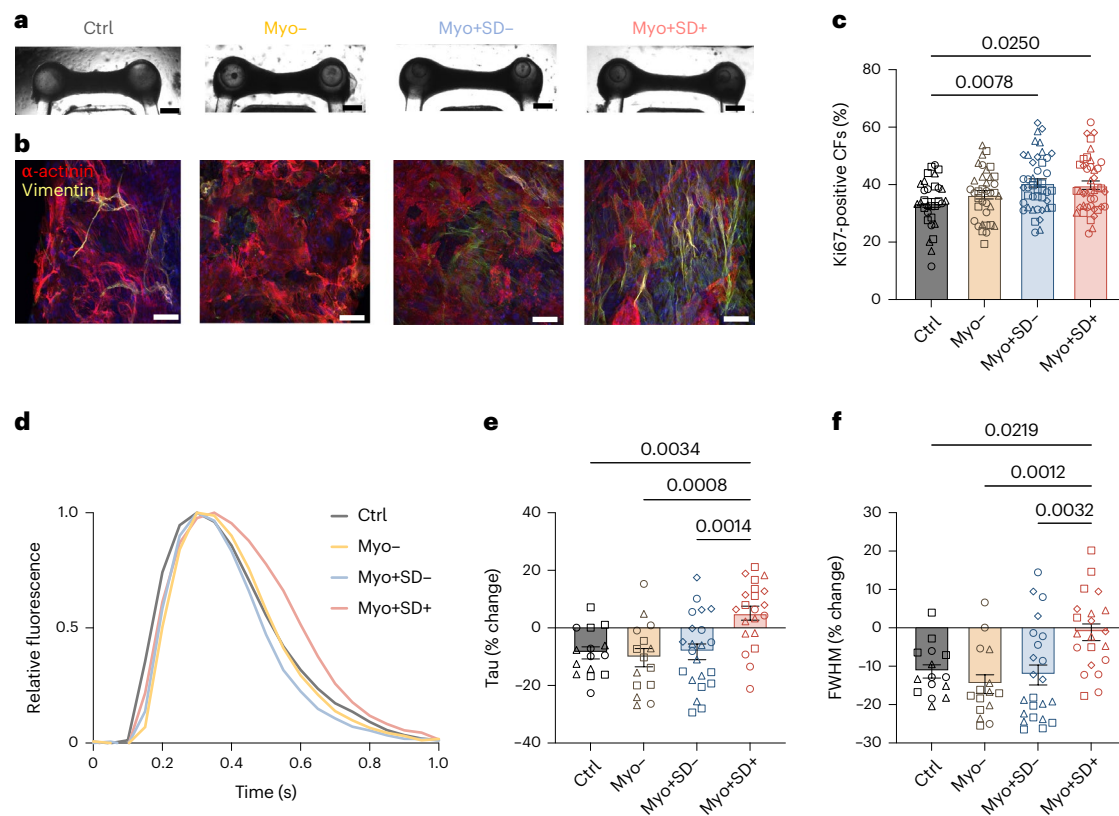
**Fig. 3 | IgGs from Myo+SD+ patients alter engineered cardiac tissue function and composition. a**, Representative bright-field images of engineered cardiac tissues after 14 days of culture with patient-specific purified IgG showing overall tissue morphology for each subgroup (scale bar, 500 μm). **b**, Representative immunofluorescence images of engineered cardiac tissue stained to show cardiomyocytes (α-actinin, red) and fibroblasts (vimentin, yellow) after 14 day culture with patient-specific IgG (scale bar, 50 μm). **c**, Quantification of the percentage of Ki-67-positive human cardiac fibroblasts after treatment with patient IgG; $n$ = 3 healthy controls, $n$ = 3 Myo− patients, $n$ = 4 Myo+SD− patients and $n$ = 4 Myo+SD+ patients ($n$ = 8–12 independent replicate wells per patient sample; exact replicate values are included in Supplementary Table 1). **d**, Representative traces of calcium flux in engineered cardiac tissues

after treatment with patient IgG. Values for each curve were normalized to the maximum value. **e,f**, Quantification of the percent change of the parameters tau (**e**) and FWHM (**f**) extracted from engineered cardiac tissue calcium transients after treatment with patient IgG compared to baseline. $n$ = 3 healthy controls, $n$ = 3 Myo− patients, $n$ = 4 Myo+SD− patients and $n$ = 4 Myo+SD+ patients ($n$ = 4–6 independent replicate tissues per patient sample; exact replicate values are included in Supplementary Table 1). Data are represented as mean ± s.e.m. Symbol shapes represent different patients within each group. Statistical significance was determined by ordinary one-way ANOVA with Tukey's test for multiple comparisons. CF, cardiac fibroblast; Ctrl, control; MFI, mean fluorescence intensity.

## Myo+SD+ IgG binding alters cardiac tissue transcriptomics

Bulk RNA sequencing (RNA-seq) identified 707 differentially expressed genes (DEGs; false discovery rate (FDR) < 0.05) between Myo+SD+ IgG-treated tissues and Myo− IgG-treated tissues and 1,035 DEGs between Myo+SD+ IgG-treated tissues and Myo+SD− IgG-treated tissues, with an overlap of 244 DEGs (Fig. 4a,b and Supplementary Table 2a,b). No DEGs were found between tissues treated with IgG from Myo+SD− and Myo− patients or between tissues treated with IgG from Myo− patients and healthy controls (Fig. 4a and Extended Data Fig. 6a). Consistent with the observed impairment in calcium handling, tissues cultured with IgG from Myo+SD+ patients exhibited reduced expression levels of genes encoding voltage-gated calcium channel subunits (*CACNB2* and *CACNA2D1*). Moreover, the expression of genes encoding cardiomyocyte transcription factors (*MEF2A* and *MEF2C*) were significantly downregulated (Extended Data Fig. 6b,c).

Principal component analysis (PCA) and hierarchical clustering analysis of gene expression of tissues cultured with patient IgG, delineated Myo+SD+ IgG-treated tissues from tissues treated with IgG from other patients with SLE and healthy controls (Fig. 4c and Extended Data Fig. 6d). Kyoto Encyclopedia of Genes and Genomes (KEGG) pathway analysis and Gene Ontology (GO) of DEGs between tissues treated with IgG from Myo+SD+ patients and Myo+SD− patients revealed terms

related to cardiomyopathies, cardiac muscle contraction and morphogenesis, adrenergic signaling, apoptosis and sarcomeric proteins (Fig. 4d and Extended Data Fig. 6e). Furthermore, we investigated cardiomyocyte-specific gene expression profiles from bulk RNA-seq data predicted by CIBERSORTx[35]. Among the DEGs between the cardiomyocyte population within tissues treated with Myo+SD+ IgG and tissues treated with Myo+SD- IgG were genes associated with mitochondria and oxidative stress. KEGG analysis of these DEGs identified pathways associated with oxidative phosphorylation, ROS and cardiomyopathy (Fig. 4e, Extended Data Fig. 7a and Supplementary Table 3). Additionally, CIBERSORTx analysis of cardiac fibroblast abundance within patient IgG-treated tissues revealed significantly larger fibroblast fraction in Myo+ IgG-treated tissues than in those treated with Myo− IgG (Extended Data Fig. 6f), consistent with the observed effects of Myo+SD+ and Myo+SD− IgG on cardiac fibroblast proliferation.

## IgGs from Myo+SD+ patients alter hiPSC-CM respiration

Based on the cardiomyocyte population transcriptomic analysis, the high metabolic demand of cardiomyocytes and the association between mitochondrial impairment and cardiac dysfunction[36–38], we sought to further investigate the effect of patient IgG on mitochondrial function. We took an orthogonal approach to quantify mitochondrial mass. First,

MitoTracker analysis showed significantly lower mitochondrial mass in hiPSC-CMs cultured with IgG from Myo+SD+ patients compared to hiPSC-CMs cultured with IgG from other patient subgroups (Fig. 4f and Extended Data Fig. 7b–d). In contrast, we found that succinate dehydrogenase (SDH) activity normalized to cell number, a metric used for indirect measurement of mitochondrial mass and/or mitochondrial biogenesis, was significantly higher in hiPSC-CMs cultured with IgG from Myo+SD+ patients (Fig. 4g). Next, oxygen consumption rate (OCR) was evaluated using the Seahorse extracellular flux assay and normalized to SDH activity to account for the differences in SDH observed across groups. Maximal respiration and spare respiratory capacity were significantly lower in the hiPSC-CMs cultured with Myo+SD+ IgG compared to hiPSC-CMs cultured with IgG from healthy controls and Myo− patients (Fig. 4h). This trend was further observed in respiratory control ratio (RCR) measurements, indicating that Myo+SD+ IgG reduced mitochondrial respiratory efficiency (Fig. 4i). Finally, using the tetramethylrhodamine methyl ester (TMRM) probe to measure mitochondrial membrane potential ($\Delta\psi m$), Myo+SD+ IgG-treated hiPSC-CMs showed a significant reduction in $\Delta\psi m$. In addition, when compared to $\Delta\psi m$ after the addition of carbonyl cyanide-p-trifluoromethoxyphenylhydrazone (FCCP) as a positive control that induces $\Delta\psi m$ depolarization, a similar trend was observed, although the effect was more pronounced with FCCP (Fig. 4j). All together, these results suggest that Myo+SD+ IgG led to reduced mitochondrial mass, respiration and respiratory efficiency, which was followed by a compensatory biogenesis mechanism as indicated by the increased SDH activity.

Cardiomyocyte metabolic dysfunction has not been previously reported in SLE, but previous studies reported that immune cells in SLE display altered metabolism[39]. Therefore, we sought to investigate whether the effect of Myo+SD+ IgG on cellular respiration would extend to peripheral blood mononuclear cells (PBMCs). Interestingly, IgGs from all SLE subgroups led to significantly lower PBMC mitochondrial content measured by MitoTracker and significantly lower maximal respiration when compared to PBMCs cultured with IgG from healthy controls (Extended Data Fig. 8a,b). Furthermore, a significant increase in SDH activity and a decrease in mitochondrial membrane potential was observed only in PBMCs cultured with IgG from the Myo+SD− and Myo+SD+ patients when compared to healthy controls (Extended Data Fig. 8c,d). Overall, similar to our findings in hiPSC-CMs, we showed that Myo+SD+ IgG altered mitochondrial content and function in PBMCs; however, in PBMCs, this effect was further extended to IgG from other SLE patient groups.

## Myo+SD+ patients exhibit unique autoantibody repertoires

Next, we sought to investigate whether the observed phenotypic and clinical variation between patients was associated with unique autoantibody signatures. We used PhIP-seq, a high-throughput unbiased technique that incorporates phage display of synthetic peptides covering the entire human proteome to characterize autoantibody reactivities at scale[40]. This method enables profiling of the full repertoire of autoantibody targets in a patient-specific manner, including both intracellular and extracellular human heart proteins. We initially validated PhIP-seq target detection by finding a linear correlation between read counts for Ro52 peptides and clinical measurements of anti-SSA/Ro autoantibodies by ELISA (Extended Data Fig. 9a). PCA of differentially detected antigen targets clearly delineated all patients with SLE from healthy controls with tight clustering among SLE patient subgroups (Fig. 5a). Thirty proteins were uniquely detected by autoantibodies present in the Myo+SD+ patients, 26 of which are expressed in the human heart at varying levels[41] (Fig. 5b, Extended Data Fig. 9b and Supplementary Table 4a). Interestingly, numerous antigens that have been reported in the literature to be targets of autoantibodies in the human heart[22,23] were identified as reactive with the IgG fractions from patients in the current study (Supplementary Table 4b). IgG from the Myo+ patients, and specifically Myo+SD+ patients, however, did not have significantly different reactivities with these antigens when compared to the other patient subgroups or healthy controls.

## Identification of candidate pathogenic autoantibodies

Based on the enhanced Myo+SD+ IgG binding to the cell surface, we sought to identify those specific surface targets. First, we characterized the cell surface proteome (surfaceome) of hiPSC-CMs and primary cardiac fibroblasts by surface biotinylation, immunoprecipitation and LC–MS/MS analysis. After data pre-processing and quality control filtering to omit intracellular proteins, we identified surface proteins unique to cardiomyocytes ($n = 27$), cardiac fibroblasts ($n = 72$) and shared by both cell types ($n = 143$) (Fig. 5c, Extended Data Fig. 9c and Supplementary Table 5). By overlapping the identified surface proteins with the 30 Myo+SD+ IgG-targeted antigens, we identified four candidate pathogenic autoantibodies. These autoantibodies targeted DIP2A, a cardiomyocyte-specific receptor associated with cardioprotection[42]; LMO7, a cardiac fibroblast-specific multifunctional regulator of protein–protein interactions[43,44]; and two surface antigens present in both cell types: PVR, associated with cell adhesion[42], and PLAUR[45], associated with extracellular matrix (ECM) degradation (Fig. 5d). Linear correlation analyses between these autoantibody read counts and EF indicated that autoantibodies to LMO7 had the strongest correlation with EF ($r^2 = 0.67$, $P = 0.002$; Fig. 5e).

## Discussion

We report a human cardiac tissue model to study autoantibody-mediated myocardial injury in SLE. Using hiPSC-CMs, cardiac fibroblasts, engineered human cardiac tissues and patient-specific autoantibody

---

**Fig. 4 | IgGs isolated from Myo+SD+ patients alter tissue transcriptomics, mitochondrial content and respiration. a**, Volcano plots depicting the DEGs between tissues cultured with patient IgG from different clinical subgroups. Statistical significance was determined by two-sided Student's *t*-test with Benjamini–Hochberg correction for multiple comparisons. Genes that were significantly upregulated (FDR < 0.05) are shown in red, and genes that were significantly downregulated (FDR < 0.05) are shown in blue. **b**, Venn diagram describing the number of DEGs between tissues treated with IgG from Myo+SD+ patients and IgG from either Myo− patients or Myo+SD− patients and the overlapping DEGs. **c**, PCA plot of global gene expression profiles for tissues treated with IgG from different patients with SLE and healthy controls. Each point represents the average expression of $n = 3$ independent tissues treated with IgG from the same patient. **d**, KEGG analysis of DEGs between tissues treated with IgG from Myo+SD+ patients and IgG from Myo+SD− patients. **e**, KEGG analysis of cardiomyocyte population DEGs between tissues treated with IgG from Myo+SD+ patients and IgG from Myo+SD− patients. **f**, Changes in hiPSC-CM mitochondrial quantity in response to patient IgG and measured by the MitoTracker Green probe. Ordinary one-way ANOVA with Dunn's post hoc comparisons test. **g**, Changes in SDH activity in hiPSC-CMs in response to patient IgG. Ordinary one-way ANOVA with Tukey's test for multiple comparisons. **h**, Characterization of IgG effect on mitochondrial respiration in hiPSC-CMs by Seahorse metabolic flux assay. OCR values were normalized to SDH activity. Ordinary two-way ANOVA with Tukey's test for multiple comparisons. **i**, Changes in hiPSC-CM RCR in response to patient IgG. Ordinary one-way ANOVA with Tukey's test for multiple comparisons. **j**, Changes in hiPSC-CM mitochondrial membrane potential in response to IgG, measured with the TMRM probe. Ordinary one-way ANOVA with Tukey's test for multiple comparisons; $^{\#}P < 0.0001$ for comparison of the FCCP group to each other patient group. Data are represented as mean ± s.e.m. $n = 3$ healthy controls, $n = 3$ Myo− patients, $n = 4$ Myo+SD− patients and $n = 4$ Myo+SD+ patients, with $n = 3$ independent tissues per patient (**a**), $n = 3$ wells per patient (**f**) or $n = 4$–6 independent replicate wells per patient sample (**g**–**j**). Exact replicate values are included in Supplementary Table 1. Symbol shapes represent different patients within each group. Ctrl, control; FC, fold change; PC, principal component; PV, *P* value.

repertoires, we identified two distinct signatures of autoantibody binding patterns that correlated with clinical phenotypes. First, IgG fractions from patients with SLE with elevated myocardial inflammation demonstrated increased binding to stressed cells within tissues subjected to electromechanical stimulation. Second, IgG from patients

with SLE with myocardial inflammation and SD (Myo+SD+) exhibited enhanced binding to the surface of live cardiomyocytes. We showed that, by binding to live cardiac cells, IgG exerted potent biological effects independent of complement and immune cell involvement. Overall, these findings indicate that SLE autoantibodies may evoke a
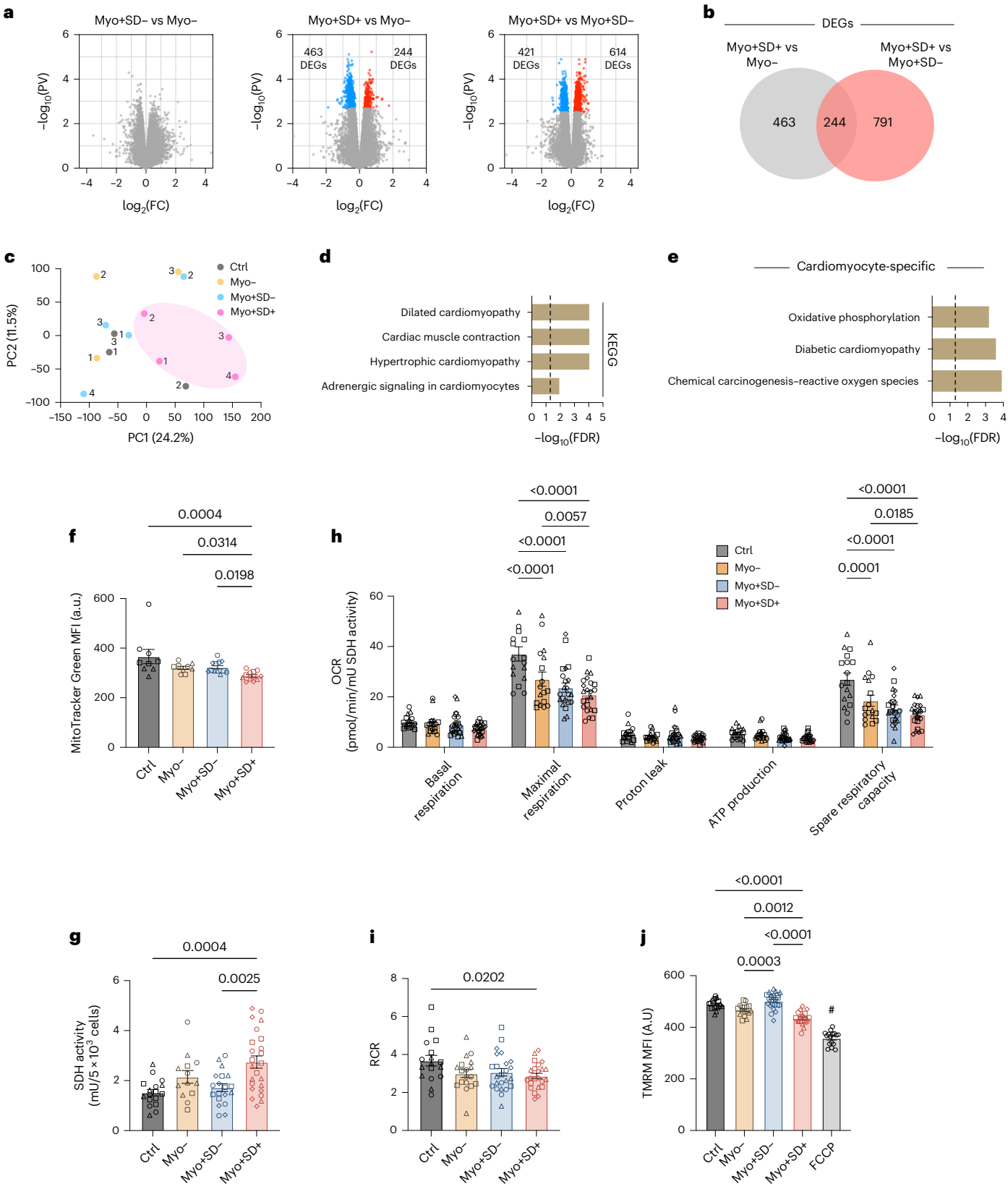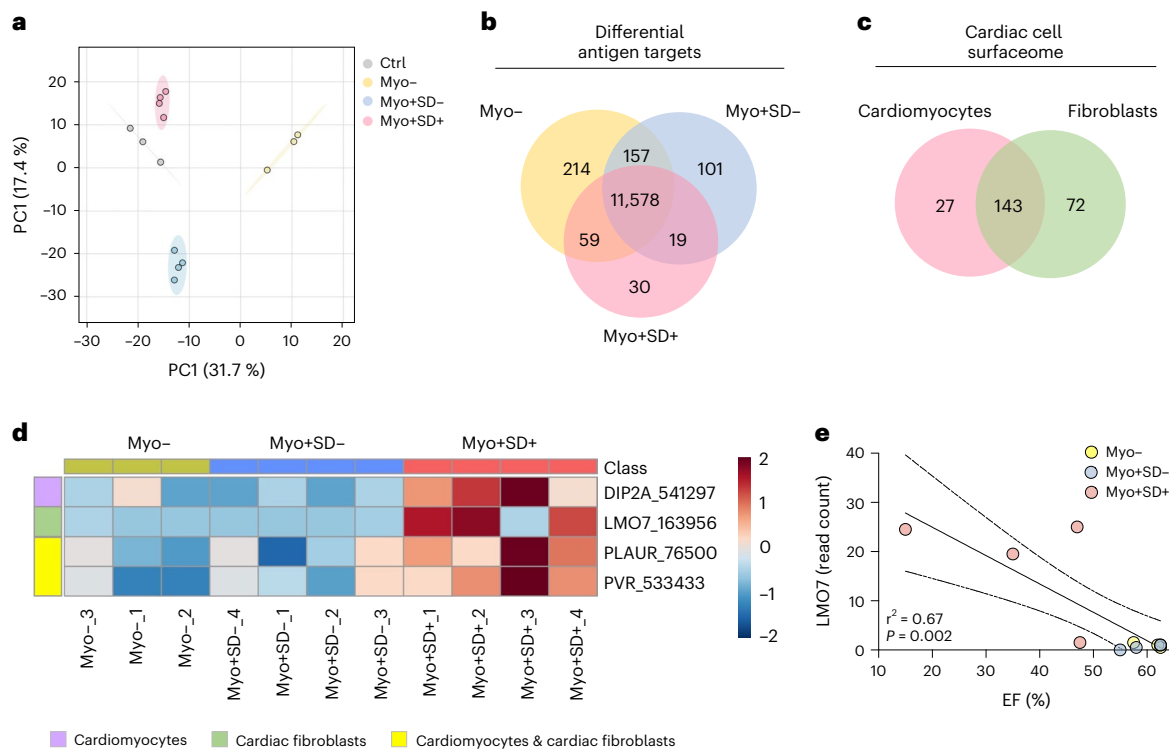
**Fig. 5 | Identification of unique and potentially pathogenic autoantibody populations in Myo+SD+ patient serum. a**, PCA plot of differential antigen targets. **b**, Venn diagram describing the number of antigen targets in each SLE patient subgroup and their overlap. **c**, Venn diagrams describing the number of cardiomyocytes and cardiac fibroblast-specific surface proteins and their overlap, representing shared surface proteins. **d**, Heatmap of potential Myo+SD+ pathogenic autoantibodies targeting cardiac cell surface antigens. **e**, Linear correlation between patient EF and corresponding read counts of LMO7. *P* value and *r*² were calculated by two-tailed Pearson's correlation analysis. Ctrl, control; PC, principal component.

range of biological processes that contribute to clinical heterogeneity in cardiac disease manifestations and outcomes.

These experiments expanded upon our previously reported engineered cardiac tissue model[28] by using metabolic maturation medium in combination with an electromechanical stimulation regimen. Using hiPSCs derived from a healthy control enabled robustness and scalability but did not account for the diverse genetic backgrounds of patients with SLE, an aspect worthy of further studies. Additionally, true autoreactivity was not demonstrated in this allogeneic model. However, the lack of binding of IgG from healthy controls to the engineered cardiac tissues suggests that the contribution of alloantibodies was minimal.

The intensity training regimen resulted in LDH release and some apoptosis likely due to oxidative stress[46]. This rendered the stressed tissues immunologically distinct from non-stressed tissues, resulting in increased IgG binding to the surface of apoptotic cells. Conversely, stress did not result in enhanced IgG binding to live cells for IgG from patients with elevated myocardial inflammation, indicating that it did not induce the presentation of newly expressed SLE antigens on their surface. Further studies are required to determine whether the increased IgG binding to the surface of apoptotic cells was due to exposed phospholipid or redistribution of intracellular antigens to the cell surface. Notably, the increased binding to apoptotic cells was consistent with previously reported SLE autoantibody binding patterns in the fetal heart and UV-damaged keratinocytes[31,47]. The correlation between enhanced autoantibody binding to stressed cardiac cells and elevated levels of myocardial inflammation suggests that such binding may evoke immune cell infiltration and activation that subsequently exacerbates myocardial inflammation. Furthermore, the similarity in patient IgG binding patterns to non-stressed cardiac tissues and healthy human heart samples underscores the advantage of our platform to model cardiac stress in vitro and identify previously unknown

associations between cardiac stress and SLE-mediated myocardial inflammation.

The lack of correlation between myocardial inflammation and SD suggests that autoantibody binding may directly influence cardiac tissue function beyond contributing to immune cell-mediated inflammation. Building upon this observation and previous studies reporting that autoantibodies can directly influence cell function in the absence of immune cells[22,25], we hypothesized that autoantibodies from patients with SD bind to the surface of cardiac cells and initiate downstream signaling or modulate physiological processes. The collected experimental evidence in this study supports this hypothesis. IgG purified from Myo+SD+ patients demonstrated enhanced binding to the surface of live cardiomyocytes, exerting potent biological effects, including altered cellular composition, respiration and tissue calcium handling and transcriptomics.

Transcriptomic analysis of cardiac tissues cultured with Myo+SD+ IgG indicated downregulation of calcium channels, supporting the observed prolonged calcium transients in those tissues. Impaired calcium handling, cytosolic calcium overload and oxidative stress in the myocardium have all been linked to dysregulation of mitochondrial function, increased mitochondrial biogenesis and the development of clinical SD[48–50]. Consistently, we found that Myo+SD+ IgG altered the expression of genes in cardiomyocytes that are associated with oxidative phosphorylation, and we further confirmed this in cellular assays. hiPSC-CMs cultured with Myo+SD+ IgG exhibited a significant decrease in mitochondrial mass, respiration and, more importantly, respiratory efficiency. Conversely, SDH activity that is classically associated with a compensatory mitochondrial biogenesis in conditions of mitochondrial dysfunction, including primary mitochondrial disorders, was increased. It remains to be established how these autoantibodies affect the different respiratory chain complexes. Importantly, considering

the abundant mitochondrial content in cardiomyocytes and the heart's high metabolic demand, the perturbation in respiration potentially renders the heart more vulnerable to IgG-induced injury compared to other organs and potentially leads to the development of SD.

Moreover, consistent with previous reports in SLE indicating altered immune cell metabolism, we found that IgG from Myo+SD+ patients altered PBMC mitochondrial content, membrane potential and respiration[39]. These findings suggest a common IgG-induced mitochondrial injury mechanism in both cell populations and indicate that impaired immune cell metabolism may further contribute to the clinical phenotype in patients with SD. Deciphering whether pharmacological interventions to modulate cardiomyocyte and immune cell metabolism would aid in the prevention of SD would be of particular interest.

The enhanced fibroblast proliferation and increased abundance within tissues cultured with Myo+ IgG and, particularly, Myo+SD+ IgG suggests that this cellular response could contribute to collagen deposition and pathological remodeling in the heart and ultimately contribute to the development of SD in (1) neonatal patients with SLE-mediated congenital heart block[51] and/or (2) adult patients with SLE. Furthermore, these data indicate that IgG-mediated injury in the heart affects multiple cell types, emphasizing the advantage of the reported tissue model. As the observed fibroblast phenotype was induced by IgG obtained from all Myo+ patients and does not fully explain the development of clinical SD, further studies looking into the effect of autoantibodies on a combined model of cardiac tissues and immune cells may uncover valuable insights into disease pathogenesis.

PhIP-seq is a powerful method for the discovery of autoantibody targets in a patient-specific manner. Despite the highly heterogenous nature of SLE and the wide array of autoantibodies in patients, we found several shared autoantibodies across all Myo+SD+ patients. By combining PhIP-seq and cell surfaceome analyses, we uncovered four new potential pathogenic autoantibodies targeting the surface of cardiomyocytes and cardiac fibroblasts, previously unlinked to autoimmune-mediated heart disease. The cardiomyocyte-enriched IgG target DIP2A is a cell surface receptor for follistatin-like 1 (FSTL1), a protein that increases cardiomyocyte survival and decreases cardiomyocyte apoptosis and hypertrophy[42,52–56]. Thus, an autoantibody to the FSTL1 receptor may interfere with its cardioprotective role and potentially contribute to the SD in Myo+SD+ patients. The cardiac fibroblast-specific protein LMO7 participates in the regulation of transforming growth factor beta (TGF-β) and fibrotic remodeling[57]. Autoantibody-mediated inhibition of LMO7 could increase fibroblast activation and proliferation, accounting for our findings in IgG-treated tissues. PLAUR, a urokinase plasminogen activator surface receptor, has established roles in ECM proteolysis, a key process in fibrotic remodeling[58], further connecting specific autoantibody targeting with fibrosis. Knockdown of PLAUR also impairs mitochondrial function, promotes immature biogenesis of mitochondria and alters cell metabolism[59–61], possibly contributing to the observed metabolic dysfunction. Given the biology of SLE, it is likely that these autoantibodies work in concert to induce injury. Further investigation of the mechanisms by which they collectively contribute to SD is required.

Although our patient IgG fractions did include some autoantibodies previously reported to be cardiac disease associated, these autoantibodies were not specifically enriched in any of the patient groups studied here, suggesting that myocardial injury in SLE is mediated by different autoantibodies than in other conditions affecting the heart. Notably, although the PhIP-seq method is limited by its ability to inform on autoantibody cross-reactivity, we used cellular assays to rule out IgG cross-reactivity with β-adrenergic receptors as a possible mechanism of injury in our study. Studies of larger patient cohorts are required to advance autoantibody–phenotype associations. Notably, anti-phospholipid autoantibodies were present in certain patients in the cohort, and it is possible that they led to valve damage that subsequently contributed to myocardial damage. Finally, exploring the effect of whole sera on cardiac tissue phenotype would be valuable to discover additional components that may lead to cardiac damage in SLE.

In conclusion, our study demonstrates the utility of an engineered model of the human myocardium for elucidating the heterogeneity and pathophysiology of autoantibody-mediated myocardial injury in patients with SLE. We envision that this model will improve myocardial risk stratification in SLE, facilitate the identification of new therapeutic targets and be extended to other diseases associated with complex autoantibody-mediated tissue damage.

## Methods

### Patient cohort

All study participants signed an informed consent form and were not compensated. The study was approved by the Columbia University Institutional Review Board (IRB). Patients were recruited from the Columbia University Lupus Center in two groups: one investigating the presence of myocardial inflammation (defined by ^{18}F-FDG myocardial uptake) in non-hospitalized patients with SLE without active cardiac symptoms and the other investigating hospitalized patients with SLE evaluated with ^{18}F-FDG PET/CT after active cardiac symptoms. Patients were 18 years of age or older and met the 1997 ACR classification criteria for SLE[32]. Patients with SLE with both myocardial inflammation and SD were included in the study only if review of previous EF measurements revealed an acute decline in EF at the time of enrollment and serum collection. Patients did not undergo endomyocardial biopsies.

### Clinical covariates

SLE disease duration was defined as the duration in years from the date of physician diagnosis. SLE disease activity was calculated using the Systemic Lupus Erythematosus Disease Activity Index 2000 (SLEDAI-2K)[62]. Traditional cardiovascular risk factors, history of lupus nephritis and antiphospholipid antibody syndrome, as well as use of immunosuppressants, were ascertained by patient questionnaire and medical record review.

### Laboratory covariates

Autoantibodies, including antinuclear antibodies, anti-SSA/Ro, anti-SSB/La, anti-dsDNA, anti-Smith and antiphospholipid antibodies, and other pertinent laboratory values, such as complement levels (C3 and C4), erythrocyte sedimentation rate (ESR) and high-sensitivity C-reactive protein, troponin and pro-beta-natriuretic peptide (pro-BNP) levels, were assessed at the clinical laboratory at New York Presbyterian Hospital and the Core Laboratory of the Columbia University Irving Institute for Clinical and Translation Research.

### ^{18}F-FDG PET/CT

Myocardial uptake imaging was performed on an MCT 64 PET/CT scanner (Siemens Medical Solutions). A low-dose CT transmission scan (120 kV, 25 mA) was obtained for attenuation correction of PET data. All patients were on a carbohydrate-free diet for 24 h. Patients were injected with $10 \pm 0.1$ mCi of ^{18}F-FDG intravenously using an antecubital or dorsal forearm catheter. A list mode three-dimensional PET scan was acquired for 10 min after a 90-min uptake period after ^{18}F-FDG injection. Non-gated attenuation-corrected images were reconstructed yielding 3-mm effective resolution. Corridor 4DM software was used to visually assess myocardial ^{18}F-FDG uptake and to semi-automatically quantify mean radiotracer uptake in the myocardium. Quantification of inflammation by ^{18}F-FDG PET/CT involved measurement of SUV in the myocardium. SUV was determined for 17 myocardial segments, and the maximum of these values was determined as SUVmax. SUVmax > 1.5 was the threshold used to define the presence of myocardial inflammation. Uptake of myocardial ^{18}F-FDG was not quantified in three patients within the cohort; instead, the presence of myocardial inflammation

was assessed qualitatively by a nuclear cardiologist and determined to be either positive or negative.

### Isolation of patient IgG fractions

Samples of serum were collected from patients at the time of ^{18}F-FDG PET/CT scans and stored at −80 °C until IgG purification. The IgG antibody fractions were isolated from patient sera by affinity purification with immobilized protein A/G using a NAb Protein A/G Spin Kit (Thermo Fisher Scientific, 89950) according to the manufacturer's protocol. Next, Zeba spin desalting columns (Thermo Fisher Scientific, 87766) were used to further purify IgG from contaminates. Notably, IgG purification from the patients' sera was performed to eliminate confounding effects of sera components, such as cytokines, growth factors and drugs. Purified IgG fractions were stored at −80 °C until experimental use.

### hiPSC sourcing

The experiments were performed using the WTC11-GCaMP6f hiPSC line, obtained through an institutional material transfer agreement with the Gladstone Institutes in San Francisco, California (Bruce Conklin)[63]. The line contains a constitutively expressed GCaMP6f calcium-responsive fluorescent protein[64] inserted into a single allele of the *AAVS1* safe harbor locus, which enables real-time and label-free visualization of calcium handling. The parental hiPSC line WTC11 (GM25256 at the Coriell Institute) was generated from a healthy donor with no history of cardiovascular or autoimmune diseases[65].

### hiPSC culture

hiPSCs were cultured in mTeSR Plus medium (STEMCELL Technologies, 100-0276) on tissue culture plates coated with Matrigel (Corning, 354230; diluted 1:100 in RPMI 1640 medium) and passaged every 3–4 d with 0.5 mM EDTA (Thermo Fisher Scientific, 15575). For the first 24 h after passaging, 5 µM Y-27632 dihydrochloride (Tocris Bioscience, 1254), a rho-associated protein kinase (ROCK) inhibitor, was added to the culture medium. hiPSCs were karyotyped and regularly tested for mycoplasma contamination.

### Cardiomyocyte differentiation from hiPSCs

Cardiomyocytes were differentiated as previously described[66]. In brief, hiPSCs were plated at a density of 155,000 cells per $cm^2$ 2 d before the start of differentiation. Culture medium was replaced with cardiomyocyte differentiation medium (CDM), consisting of RPMI 1640 medium (Thermo Fisher Scientific, A4192302), 500 µg $ml^{-1}$ recombinant human albumin (Sigma-Aldrich, A9731) and 213 µg $ml^{-1}$ L-ascorbic acid 2-phosphate (Sigma-Aldrich, A8960). From day 0 to day 2, CDM was supplemented with 4 µM CHIR99021 (Tocris Bioscience, 4423), and, from day 2 to day 4, CDM was supplemented with 2 µM Wnt-C59 (Tocris Bioscience, 5148). After this, CDM was changed every 2 days. On day 10, CDM was replaced with purification medium, consisting of RPMI 1640 without glucose (Thermo Fisher Scientific, 11879020), B27 Supplement (Thermo Fisher Scientific, 17504044, 1×) and 213 µg $ml^{-1}$ L-ascorbic acid 2-phosphate, to purify the hiPSC-CM population and eliminate potential contaminating cell populations. On day 13, the medium was replaced with RPMI-B27 medium, consisting of RPMI 1640 medium, B27 Supplement 1× and 213 µg $ml^{-1}$ L-ascorbic acid 2-phosphate. On day 17, cells were pre-treated with 5 µM Y-27632 dihydrochloride for 4 hours to prepare for dissociation. Cells were dissociated by enzyme digestion with 95 U $ml^{-1}$ collagenase type II (Worthington, LS004176) and 0.6 mg $ml^{-1}$ pancreatin (Sigma-Aldrich, P7545) in a dissociation buffer consisting of 5.5 mM glucose, 1.8 mM $CaCl_2$, 5.4 mM KCl, 0.81 mM $MgSO_4$, 100 mM NaCl, 44 mM $NaHCO_3$ and 0.9 mM $NaH_2PO_4$. Cells were incubated at 37 °C on a shaker for approximately 30 min. Flow cytometry for cardiac troponin T (cTnT; BD Biosciences, 565744) was performed before cell use for tissue fabrication to ensure cell purity (>90% cTnT+).

### Cardiac fibroblasts

Primary human ventricular cardiac fibroblasts (NHCF-V; Lonza, CC-2904) were cultured according to the manufacturer's protocol with Fibroblast Growth Medium 3 (PromoCell, C-23130). Fibroblasts were used between passage 3 and passage 5. Cells were generated from healthy donors with no history of autoimmune or cardiovascular disease.

### PBMCs

Human PBMCs (STEMCELL Technologies, 70025.2) were cultured in RPMI 1640 with 10% heat-inactivated FBS according to the manufacturer's protocol.

### Human LV tissue samples

De-identified human LV tissue samples were obtained from the Columbia University Biobank for Translational Studies under IRB protocol number AAAR6796.

### milliPillar platform fabrication

The platform, termed milliPillar, was assembled as previously described[28]. In brief, the platform was fabricated by casting polydimethylsiloxane (PDMS; Dow Chemical Company, 02065622; 1:10 curing agent-to-elastomer ratio) into custom molds containing carbon electrodes and curing overnight at 65 °C. The platform was then detached from the mold and plasma bonded to a glass slide. After completion, each well contained a set of horizontal flexible pillars upon which fibrin hydrogel containing cells can be suspended, as described below. Each well also contained a set of carbon electrodes for electrical field stimulation. A custom microcontroller-based electrical stimulator was used for electrical pacing during culture and video acquisition, as previously described[28].

### Human engineered cardiac tissues

Engineered cardiac tissues were fabricated as previously described[28]. In brief, dissociated hiPSC-CMs and primary cardiac fibroblasts were mixed in a 3:1 ratio and resuspended in fibrinogen by mixing the cell solution with 33 mg $ml^{-1}$ human fibrinogen (Sigma-Aldrich, F3879) and RPMI-B27 (described above) to a final fibrinogen concentration of 5 mg $ml^{-1}$ and cell concentration of 37,000 cells per microliter. A 3-µl drop of 2.5 U $ml^{-1}$ human thrombin (Sigma-Aldrich, T6884) was added to each platform well, followed by addition of 12 µl of the cell–fibrinogen solution. The two solutions were mixed, spread evenly across the well and incubated at 37 °C for 15 min, allowing the fibrin hydrogel to polymerize within the well. After polymerization, each well was filled with 400 µl of RPMI-B27 supplemented with 10 µM Y-27632 and 5 mg $ml^{-1}$ 6-aminocaproic acid (Sigma-Aldrich, A7824). On day 1, RPMI-B27 medium was replaced without Y-27632.

### Optimization of engineered cardiac tissue culture medium

On day 2, platforms were randomized into two different culture medium groups: RPMI-B27 and a previously reported metabolic MM[34]. Medium also contained 6-aminocaproic acid and was changed every other day. On day 6, 6-aminocaproic acid was removed from the culture medium. On day 7, electrical stimulation was initiated at a frequency of 2 Hz until day 14. Tissue functionality was assessed by calcium and bright-field imaging on day 14. Force generation, contraction and relaxation velocities and calcium transient amplitude and kinetics were measured (Extended Data Fig. 4). Tissues cultured in MM displayed enhanced structural and functional properties; therefore, MM was chosen as the culture medium for subsequent experiments with patient IgG.

### Engineered cardiac tissue incubation with autoantibodies

Engineered cardiac tissues cultured in MM were fabricated as described above, and, at day 7, a 14 day gradually increasing electromechanical

stimulation regimen (2 Hz to 6 Hz, 'intensity training') was initiated. Patient-specific serum purified IgG was added 7 d after the initiation of the electromechanical stimulation regimen when frequency reached 4 Hz and was maintained for an additional 14 days. To ensure that the functional effect on cardiac tissue performance is not associated to titer levels and only to distinct autoantibody patterns, the same concentration of purified patient autoantibodies, 0.5 μg ml⁻¹, was added to all tissues. To assess the effect of purified IgG on cardiac tissue functionality, we evaluated the tissue contractility and calcium handling (the full list of metrics and their descriptions is provided in Extended Data Fig. 4) at baseline (day 14) and after the addition of IgG, on days 21 and 28. To reduce noise from tissue-to-tissue variability, measurements were normalized to the baseline.

### Indirect immunostaining to visualize IgG targets

Cardiac tissues and hiPSC-CMs cultured with patient IgG were fixed in 4% paraformaldehyde, blocked for 1 hour at room temperature in PBS with 2% FBS and subsequently incubated with secondary anti-human IgG (1:500, Thermo Fisher Scientific, A21090, or Sigma Aldrich, SAB4600181). This method enabled visualization of cellular antigens accessible to autoantibodies only in live tissues or cells. Samples were visualized using a scanning laser confocal microscope (A1 confocal system with Eclipse Ti inverted microscope, Nikon Instruments). Binding intensity was measured by image analysis in ImageJ. IgG binding levels were quantified as MFI.

### Immunostaining

Whole-mount engineered cardiac tissues and cells were fixed and permeabilized in 100% ice-cold methanol for 10 min, washed three times in PBS and then blocked for 1 hour at room temperature in PBS with 2% FBS. After blocking, the tissues were incubated with primary mouse anti-α-actinin (sarcomeric) antibody (1:750, Sigma-Aldrich, A7811) and vimentin (1:2,500, Abcam, ab24525), washed three times and incubated for 1 hour with secondary antibodies (Thermo Fisher Scientific, A-11039, A11041, A31571 and A11030). For nuclei detection, the tissues were washed and incubated with NucBlue (Thermo Fisher, Scientific, R37606). Whole tissues were placed in incubation chambers (Grace Bio-Labs, 645501) and mounted with ProLong Diamond antifade mountant (Invitrogen, 36961). Tissues were visualized using a scanning laser confocal microscope (A1 confocal system with Eclipse Ti inverted microscope, Nikon Instruments).

### Flow cytometry to assess autoantibody binding

hiPSC-CMs were differentiated and dissociated as described above. Individual patient IgG samples were diluted 1:500 in cell staining buffer (BioLegend, 420201) and incubated with hiPSC-CMs for 1 hour at room temperature, followed by incubation with CF-647 conjugated anti-human IgG (Sigma-Aldrich, SAB4600181) diluted 1:500 in cell staining buffer for 30 min at room temperature. hiPSC-CMs were then stained with Apotracker Green (BioLegend, 427401) and propidium iodide (Thermo Fisher Scientific, R37169) according to the manufacturers' protocols. Flow cytometry was conducted with a ZE5 Cell Analyzer (Bio-Rad) to identify live cardiomyocytes and quantify IgG binding. FlowJo software (BD Biosciences) was used for analysis. Live cardiomyocytes were defined as those with negative staining for propidium iodide, a marker of dead cells, and Apotracker Green, a marker of apoptotic cells. An example of the gating strategy is provided in Extended Data Fig. 3b. IgG binding levels were quantified as median fluorescent intensity for all cells within the viable cardiomyocyte population.

### Fibroblast imaging assays

Cardiac fibroblasts were cultured with patient IgG for 72 hours and immunostained as previously described in the Methods section to evaluate the number of Ki67-positive cells. Primary antibody against Ki-67 was used (1:100, Abcam, ab15580). Primary cells were stained with

DAPI and then imaged with a high-throughput imaging system (BioTek Cytation 5, Agilent). Image fields with more than 200 or fewer than 95 cells were excluded from analysis.

### Calcium imaging and analysis

To decrease tissue-to-tissue variability, all metrics were measured as percent change from baseline. Tissues were imaged in a live-cell chamber (STX Temp & CO₂ Stage Top Incubator, Tokai Hit) using a sCMOS camera (Zyla 4.2, Andor Technology) connected to an inverted fluorescence microscope with a standard GFP filter set (IX-81, Olympus). Tissues were then electrically stimulated at 1 Hz, and videos were acquired at 100 frames per second (fps) for 300 frames to measure calcium transients. Calcium signals were analyzed using a previously published script[28]. In brief, the script was developed to average the pixel intensities for each frame, and this transient was then corrected for fluorescent decay. Further analysis by the script then extracted the metrics of calcium handling, including calcium amplitude, FWHM, contract 50 and the exponential decay constant ($\tau$). A description of these metrics is provided in Extended Data Fig. 4.

### MitoTracker Green assay

hiPSC-CMs were dissociated after differentiation and replated in Matrigel-coated 96-well plates at 200,000 cells per cm². After 2 weeks in culture in MM, cells were cultured with patient IgG (0.5 μg ml⁻¹) for 1 week and then assayed. For PBMC analysis, cells were thawed and cultured with patient IgG (0.5 μg ml⁻¹) for 1 week and then assayed. Cells were stained with MitoTracker Green (Thermo Fisher Scientific, M46750) according to the manufacturer's protocol, and fluorescence was measured using a ZE5 Cell Analyzer (Bio-Rad). MitoTracker Green was quantified as median fluorescence intensity.

### Measurement of mitochondrial membrane potential

hiPSC-CMs were dissociated after differentiation and replated in Matrigel-coated 96-well plates at 200,000 cells per cm². After 2 weeks in culture in MM, cells were cultured with patient IgG (0.5 μg ml⁻¹) for 1 week and then assayed. For PBMC analysis, cells were thawed and cultured with patient IgG (0.5 μg ml⁻¹) for 1 week and then assayed. Cells were incubated with 20 nM TMRM in culture medium for 30 min at 37 °C and then washed two times with PBS. For hiPSC-CMs, fluorescence was measured using a plate reader (BioTek Synergy, Agilent) with excitation and emission filters for 530 nm and 590 nm, respectively. For PBMCs, fluorescence was measured with a ZE5 Cell Analyzer (Bio-Rad). For a positive control, cells were then treated with 10 μM FCCP for 5 min, and then fluorescence was measured again.

### Metabolic analysis

An extracellular flux analyzer (Seahorse XF96, Agilent) was used with the Seahorse XF Cell Mito Stress Test assay (Agilent, 103015-100) to evaluate mitochondrial function. One week before the hiPSC-CM assay, 33,000 cardiomyocytes (GCAMP) were plated onto a Matrigel-coated Seahorse XFe96 Pro cell culture microplate (Agilent, 103794-100) in B27 + 10 μM ROCK inhibitor and, the next day, changed to MM with patient-specific IgG and then cultured for 1 week. Media were changed every other day until the day of the assay. For PBMC analysis, PBMCs were cultured for 1 week in RPMI 1640 with 1% penicillin–streptomycin, 10% heat-inactivated FBS and patient IgG. On the day of the assay, PBMCs were transferred to a Seahorse XFe96 Pro cell culture microplate coated with 0.1 mg ml⁻¹ poly-D-lysine plate and briefly centrifuged to adhere cells to the surface of each well. For both studies, 1 h before the assay, the culture medium was exchanged to assay medium (XF RPMI Medium, pH 7.4, supplemented with 1 mM pyruvate, 2 mM glutamine and 10 mM glucose), and the culture plate was placed in a non-CO₂ incubator. During the Mito Stress Test, electron transport chain modulators oligomycin (1.5 μM), FCCP (0.5 μM) and rotenone and antimycin A (0.5 μM) were injected serially into each well. The key parameters of mitochondrial

function determined by the Mito Stress Test, including basal respiration, ATP-linked respiration, proton leak, maximal respiration, spare capacity and non-mitochondrial oxygen consumption, were generated using the Seahorse XF Mito Stress Test Report Generator. After Seahorse assay, cells were stained with NucBlue live ready probes (Invitrogen, R37605) and imaged with an inverted fluorescence microscope with a standard GFP filter set (IX-81, Olympus) as well as in bright-field. Cell number was quantified using FIJI. After Seahorse assay, an SDH activity assay (Abcam, ab228560) was performed according to the manufacturer's protocol.

## Contractile function

For force generation measurements, videos were acquired at 20 fps for 4,800 frames using a custom program to stimulate cardiac tissues from 0.5 Hz to 4 Hz as previously described, and force generation was analyzed from bright-field videos as previously described[28]. In brief, a custom Python script was developed to track the motion of the pillar heads and to calculate the force by multiplying the displacement of the pillars with the coefficient determined from the force-displacement calibration curve generated for the pillars. The script used the location of the pillar heads to determine the total deflection of the pillar from their equilibrium position without any force applied. Further analysis of the deflection trace extracted metrics of contractility, including the following: force, passive force, active force, contraction velocity and relaxation velocity. A description of these metrics is provided in Extended Data Fig. 4. To decrease tissue-to-tissue variability, all metrics were measured as percent change from baseline.

## Analysis of tissue function

After feature extraction, tissues that did not capture at 1-Hz stimulation based on both calcium and contractility analysis at baseline were removed from further analysis. The data were then processed to remove outliers greater than or less than ±1.5× the interquartile range for each group. Outliers were removed from each metric independently. The metrics for each tissue were internally normalized to baseline values and presented as percent change from baseline.

## RNA isolation

Tissues were snap frozen in liquid nitrogen and stored at −80 °C until use. To isolate RNA, snap-frozen tissues were added to 300 µl of RNA lysis buffer with a stainless steel bead (BioSpec, 11079123) and homogenized with a Mini-BeadBeater (BioSpec, C321001) for 5–10 s or until tissue samples were not visible. RNA was then isolated using a Qiagen RNeasy Micro Kit (Qiagen, 74004) according to the manufacturer's instructions. RNA for each sample was then analyzed for quality/quantity using an Agilent Bioanalyzer, Qubit 2.0, at Columbia's Molecular Pathology Core.

## RNA-seq

The SMART-Seq version 4 Ultra Low Input RNA Kit for Sequencing (TaKaRa) was used for cDNA amplification according to the manufacturer's instructions. The sequencing library was prepared using the Nextera XT DNA Library Preparation Kit (Illumina) with 100–150 pg of starting material and according to the manufacturer's instructions. Libraries were sequenced to a targeted depth of approximately 40 M 100-bp paired-end reads on a NovaSeq 6000. RTA (Illumina) was used for base calling and bcl2fastq2 (version 2.19) for converting BCL to FASTQ format, coupled with adaptor trimming.

## RNA-seq analysis

RNA-seq reads were quantified with Kallisto[67], using the Ensembl v96 Human:GRCh38.p12 transcriptome as a reference. Data were deposited in the Gene Expression Omnibus (GSE227571). Multidimensional scaling[68], PCA[69] and hierarchical clustering[70] were used to check for outliers. Samples were normalized by the Trimmed Mean Method[71]. Differential expression was analyzed with limma-voom with sample weighting[72–74] and duplicate correlation[75], which models the effect of three tissue samples per patient IgG sample. Differential expression results were analyzed with KEGG[76] and GO Biological Process[77], using a significance cutoff of $P < 0.001$ and $|\log_2\text{fold change}| \geq 0.6$. iPathwayGuide[78] was used to perform the KEGG analysis, using the Signal Interaction Pathway (SIP) analysis[79,80] method, as well as GO analysis, using the high-specificity pruning method, which is based on the elim method[81]. CIBERSORTx was used to infer hiPSC-CM-specific gene expression profiles from bulk RNA-seq and provide an estimation of the cellular fraction of cardiomyocytes and cardiac fibroblasts within the tissues[35].

## Surface protein analysis

Human primary cardiac fibroblasts were seeded in 10-cm dishes, and hiPSC-CMs were plated in six-well plates. Two wells were used per pull-down reaction. A Pierce Cell Surface Biotinylation and Isolation Kit (Thermo Fisher Scientific, A44390) was used per the manufacturer's protocol to biotinylate and pull down cell surface proteins with minor alterations. Before biotinylation, cells were washed four times with PBS. Biotinylation reaction was conducted for 30 min at room temperature, after which the cells were washed four times with PBS and lysed on the plate in the provided lysis buffer with 1× Halt Protease and Phosphatase Inhibitor Cocktail (Thermo Fisher Scientific, 78442). Protein concentrations were determined with a BCA assay. An equivalent amount of 1,000 µg of protein was used per pulldown reaction, and cell lysate was incubated with streptavidin beads for 2 h at room temperature. The surface proteins were eluted in 40 µl of custom elution buffer (12.5 mM biotin, 7.5 mM HEPES (pH 7.5), 75 mM NaCl, 1.5 mM EDTA, 0.15% (w/v) SDS, 0.075% (w/v) sarkosyl and 0.02% (w/v) Na-deoxycholate) at room temperature for 30 min and an addition of 40 µl of custom elution buffer at 65 °C for 20 min. Subsequently, 30 µl was used for western blot confirmation, and the remaining 50 µl was analyzed with mass spectrometry.

## Global surface protein quantitative analysis

For global surface protein quantitative analysis of cardiac fibroblasts and cardiomyocytes, the diaPASEF-based method was used[82]. In brief, the eluted proteins from streptavidin beads were denatured in SDC buffer (1% SDC, 100 mM Tris-HCl, pH 8.5) and boiled for 20 min at 60 °C and 1,000 r.p.m. Protein reduction and alkylation of cysteines were performed with 10 mM TCEP and 40 mM CAA at 45 °C for 20 min, followed by sonication in a water bath and cooled down to room temperature. Proteins were precipitated with the SP3 method, as previously described[83], and SP3 beads were resuspended in SDC buffer (1% SDC/100 mM Tris, pH 8.5). Protein digestion was processed overnight by adding LysC:trypsin mix in a 1:50 ratio (µg of enzyme to µg of protein) at 37 °C and 1,400 r.p.m. Peptides were acidified by adding 1% TFA, vortexed, subjected to StageTip cleanup via SDB-RPS2 and dried in a speed-vac. Peptides were resuspended in 10 µl of LC buffer (3% acetonitrile (ACN)/0.1% formic acid (FA)). Peptide concentrations were determined using NanoDrop, and 200 ng of each sample was used for diaPASEF analysis on a timsTOF Pro.

## LC–MS/MS for surface protein characterization

Peptides were separated within 87 min at a flow rate of 400 nl min$^{-1}$ on a reversed-phase C18 column with an integrated CaptiveSpray emitter (25 cm × 75 µm, 1.6 µm, IonOpticks). Mobile phases A and B were with 0.1% FA in water and 0.1% FA in ACN. The fraction of B was linearly increased from 2% to 23% within 70 min, followed by an increase to 35% within 10 min and a further increase to 80% before re-equilibration. The timsTOF Pro was operated in diaPASEF mode, and data were acquired at defined 22 × 50 Th isolation windows from $m/z$ 440 to 1,440. Two IM windows per diaPASEF scan were set. The collision energy was ramped linearly as a function of the mobility from 59 eV at 1/K0 = 1.6 Vs/cm$^2$ to 20 eV at 1/K0 = 0.6 Vs/cm$^2$. The acquired diaPASEF raw files were searched with the UniProt Human proteome database (UP000005640) in the DIA-NN search engine with default

settings of the library-free search algorithm[84]. DIA-NN performed the search trypsin digestion with up to two missed cleavages. The following modifications were used for protein identification and quantification: carbamidomethylation of cysteine residues (+57.021 Da) was set as static modifications, and acetylation of the protein N-terminus (+42.010) and oxidation of methionine residues (+15.995 Da) was set as a variable modification. The FDR was set to 1% at the peptide precursor and protein level. Results obtained from DIA-NN were further analyzed using Perseus software[85]. Significantly changed protein candidates were determined by $t$-test with a threshold for significance of $P < 0.05$ (permutation-based FDR correction) and 0.58 $\log_2$fold change. Because isolation procedures may yield some contaminating cells with compromised plasma membranes, a further validation step of the significant proteins was performed, and data were compared to three subcellular localization data sources—Human Protein Atlas[86], Jensen Lab Compartment Repository[87] and CellSurfer[88]—for further quality control (Extended Data Fig. 7a).

### PhIP-seq analysis

PhIP-seq analysis and sequencing were performed according to previous publications[40,89], with a few modifications. Sera containing approximately 100 µg of IgG (quantified using a Human IgG ELISA Quantification Set, Bethyl Laboratories) were added to each well, in duplicate, combined with 1 ml of Human PhIP-seq library[40] diluted to approximately $2 \times 10^5$ fold representation in phage extraction buffer (20 mM Tris-HCl, pH 8.0, 100 mM NaCl, 6 mM MgSO$_4$). After incubation, phages were pulled down using anti-FLAG magnetic beads. IgGs that did not bind to phages were discarded, and, after washing and releasing of complex phage IgG from beads, IgGs bound to phages were pulled down using anti-protein A and protein G magnetic beads. Phage DNA was extracted by incubation at 95 °C for 10 min.

The DNA for multiplexed Illumina sequencing was prepared after two rounds of amplification using Q5 Hot Star Polymerase (New England Biolabs). For the first round of polymerase chain reaction (PCR), we used the primers IS7 (ACACTCTTTCCCTACACGACTCCAGTCAG-GTGTGATGCTC) and IS8 (GTGACTGGAGTTCAGACGTGTGCTCTTC-CGATCCGAGCTTATCGTCGTCATCC), and, for the second round, we used primer IS4 (AATGATACGGCGACCACCGAGATCTACACTCTTTC-CCTACACGACTCCAGT) and a different unique indexing primer for each sample to be multiplexed for sequencing. Equimolar amounts of all samples were pooled, gel purified and sequenced by the Harvard Medical School Biopolymers Facility using a 50-bp read cycle on an Illumina NextSeq.

### PhIP-Seq data analysis

Read counts were normalized by z-score, and a $t$-test was applied to compare each pair of groups (SLE versus Control, Myo− versus Myo+SD−, Myo− versus Myo+SD+ and Myo+SD- versus Myo+SD+). To compare more than two pairs, one-way ANOVA test was applied. Peptides for which the comparison resulted in a $P$ value lower than 0.05 were considered different for following analyses.

### Statistical analysis and reproducibility

Statistical analyses were performed with GraphPad Prism 10.0 using unpaired two-tailed Student's $t$-test or Mann–Whitney $U$-test. Longitudinal comparison between different groups was performed by one-way or two-way ANOVA with Tukey's post test or with ordinary one-way ANOVA with Dunnett's test for multiple comparisons. For cardiac tissue functional analysis, individual beats with parameters outside of 1.5× the interquartile range were excluded as outliers. For other assays, Tukey's test for outlier exclusion was used with GraphPad Prism 10.0. For representative immunofluorescence images presented in the manuscript, a minimum of three biological replicates (individual experiments) and three technical replicates (images) were used to select a reproducible and representative image.

### Reporting Summary

Further information on research design is available in the Nature Portfolio Reporting Summary linked to this article.

## References

1.  Guglin, M., Smith, C. & Rao, R. The spectrum of lupus myocarditis: from asymptomatic forms to cardiogenic shock. *Heart Fail. Rev.* **26**, 553–560 (2021).
2.  Appenzeller, S., Pineau, C. A. & Clarke, A. E. Acute lupus myocarditis: clinical features and outcome. *Lupus* **20**, 981–988 (2011).
3.  Thomas, G. et al. Lupus myocarditis: initial presentation and longterm outcomes in a multicentric series of 29 patients. *J. Rheumatol.* **44**, 24–32 (2017).
4.  Bartels, C. M. et al. Mortality and cardiovascular burden of systemic lupus erythematosus in a US population-based cohort. *J. Rheumatol.* **41**, 680–687 (2014).
5.  Hak, A. E., Karlson, E. W., Feskanich, D., Stampfer, M. J. & Costenbader, K. H. Systemic lupus erythematosus and the risk of cardiovascular disease: results from the Nurses' Health Study. *Arthritis Rheum.* **61**, 1396–1402 (2009).
6.  Aldajani, A. & Chetrit, M. Editorial commentary: Myocardial involvement in systemic lupus erythematosus—more than the MR-eye can see. *Trends Cardiovasc. Med.* **33**, 355–356 (2023).
7.  Winau, L. et al. High-sensitive troponin is associated with subclinical imaging biosignature of inflammatory cardiovascular involvement in systemic lupus erythematosus. *Ann. Rheum. Dis.* **77**, 1590–1598 (2018).
8.  Knight, J. S. & Kaplan, M. J. Cardiovascular disease in lupus: insights and updates. *Curr. Opin. Rheumatol.* **25**, 597–605 (2013).
9.  Miner, J. J. & Kim, A. H. Cardiac manifestations of systemic lupus erythematosus. *Rheum. Dis. Clin. North Am.* **40**, 51–60 (2014).
10. Suurmond, J. & Diamond, B. Autoantibodies in systemic autoimmune diseases: specificity and pathogenicity. *J. Clin. Invest.* **125**, 2194–2202 (2015).
11. Salomonsson, S. et al. Ro/SSA autoantibodies directly bind cardiomyocytes, disturb calcium homeostasis, and mediate congenital heart block. *J. Exp. Med.* **201**, 11–17 (2005).
12. Xiao, G. Q., Hu, K. & Boutjdir, M. Direct inhibition of expressed cardiac L- and T-type calcium channels by IgG from mothers whose children have congenital heart block. *Circulation* **103**, 1599–1604 (2001).
13. Karnabi, E. et al. Congenital heart block: identification of autoantibody binding site on the extracellular loop (domain I, S5–S6) of α$_{1D}$ L-type Ca channel. *J. Autoimmun.* **34**, 80–86 (2010).
14. Boutjdir, M. et al. Serum and immunoglobulin G from the mother of a child with congenital heart block induce conduction abnormalities and inhibit L-type calcium channels in a rat heart model. *Pediatr. Res.* **44**, 11–19 (1998).
15. Buyon, J. P. & Winchester, R. Congenital complete heart block. A human model of passively acquired autoimmune injury. *Arthritis Rheum.* **33**, 609–614 (1990).

16. Schulze, K., Becker, B. F., Schauer, R. & Schultheiss, H. P. Antibodies to ADP-ATP carrier–an autoantigen in myocarditis and dilated cardiomyopathy–impair cardiac function. *Circulation* **81**, 959–969 (1990).

17. Warraich, R. S. et al. Human cardiac myosin autoantibodies impair myocyte contractility: a cause-and-effect relationship. *FASEB J.* **20**, 651–660 (2006).

18. Okazaki, T. et al. Autoantibodies against cardiac troponin I are responsible for dilated cardiomyopathy in PD-1-deficient mice. *Nat. Med.* **9**, 1477–1483 (2003).

19. Wang, L. et al. Decreased autophagy induced by β$_1$-adrenoceptor autoantibodies contributes to cardiomyocyte apoptosis. *Cell Death Dis.* **9**, 406 (2018).

20. Xiao, H. et al. Arrhythmogenic autoantibodies against calcium channel lead to sudden death in idiopathic dilated cardiomyopathy. *Eur. J. Heart Fail.* **13**, 264–270 (2011).

21. Kill, A. et al. Autoantibodies to angiotensin and endothelin receptors in systemic sclerosis induce cellular and systemic events associated with disease pathogenesis. *Arthritis Res. Ther.* **16**, R29 (2014).

22. Kaya, Z., Leib, C. & Katus, H. A. Autoantibodies in heart failure and cardiac dysfunction. *Circ. Res.* **110**, 145–158 (2012).

23. Ryabkova, V. A. et al. Lethal immunoglobulins: autoantibodies and sudden cardiac death. *Autoimmun. Rev.* **18**, 415–425 (2019).

24. Lazzerini, P. E., Capecchi, P. L., Laghi-Pasini, F. & Boutjdir, M. Autoimmune channelopathies as a novel mechanism in cardiac arrhythmias. *Nat. Rev. Cardiol.* **14**, 521–535 (2017).

25. DeGiorgio, L. A. et al. A subset of lupus anti-DNA antibodies cross-reacts with the NR2 glutamate receptor in systemic lupus erythematosus. *Nat. Med.* **7**, 1189–1193 (2001).

26. Faust, T. W. et al. Neurotoxic lupus autoantibodies alter brain function through two distinct mechanisms. *Proc. Natl Acad. Sci. USA* **107**, 18569–18574 (2010).

27. Ronaldson-Bouchard, K. et al. Advanced maturation of human cardiac tissue grown from pluripotent stem cells. *Nature* **556**, 239–243 (2018).

28. Tamargo, M. A. et al. milliPillar: a platform for the generation and real-time assessment of human engineered cardiac tissues. *ACS Biomater. Sci. Eng.* **7**, 5215–5229 (2021).

29. Casciola-Rosen, L. & Rosen, A. Ultraviolet light-induced keratinocyte apoptosis: a potential mechanism for the induction of skin lesions and autoantibody production in LE. *Lupus* **6**, 175–180 (1997).

30. Casciola-Rosen, L. A., Anhalt, G. & Rosen, A. Autoantigens targeted in systemic lupus erythematosus are clustered in two populations of surface structures on apoptotic keratinocytes. *J. Exp. Med.* **179**, 1317–1330 (1994).

31. Miranda, M. E. et al. Accessibility of SSA/Ro and SSB/La antigens to maternal autoantibodies in apoptotic human fetal cardiac myocytes. *J. Immunol.* **161**, 5061–5069 (1998).

32. Hochberg, M. C. Updating the American College of Rheumatology revised criteria for the classification of systemic lupus erythematosus. *Arthritis Rheum.* **40**, 1725 (1997).

33. Perel-Winkler, A. et al. Myocarditis in systemic lupus erythematosus diagnosed by ^{18}F-fluorodeoxyglucose positron emission tomography. *Lupus Sci. Med.* **5**, e000265 (2018).

34. Feyen, D. A. M. et al. Metabolic maturation media improve physiological function of human iPSC-derived cardiomyocytes. *Cell Rep.* **32**, 107925 (2020).

35. Newman, A. M. et al. Determining cell type abundance and expression from bulk tissues with digital cytometry. *Nat. Biotechnol.* **37**, 773–782 (2019).

36. Ranjbarvaziri, S. et al. Altered cardiac energetics and mitochondrial dysfunction in hypertrophic cardiomyopathy. *Circulation* **144**, 1714–1731 (2021).

37. Ramaccini, D. et al. Mitochondrial function and dysfunction in dilated cardiomyopathy. *Front. Cell Dev. Biol.* **8**, 624216 (2020).

38. Remondino, A. et al. β-adrenergic receptor-stimulated apoptosis in cardiac myocytes is mediated by reactive oxygen species/c-Jun NH2-terminal kinase–dependent activation of the mitochondrial pathway. *Circ. Res.* **92**, 136–138 (2003).

39. Morel, L. Immunometabolism in systemic lupus erythematosus. *Nat. Rev. Rheumatol.* **13**, 280–290 (2017).

40. Larman, H. B. et al. Autoantigen discovery with a synthetic human peptidome. *Nat. Biotechnol.* **29**, 535–541 (2011).

41. Litvinukova, M. et al. Cells of the adult human heart. *Nature* **588**, 466–472 (2020).

42. Ouchi, N. et al. DIP2A functions as a FSTL1 receptor. *J. Biol. Chem.* **285**, 7127–7134 (2010).

43. Holaska, J. M., Rais-Bahrami, S. & Wilson, K. L. Lmo7 is an emerin-binding protein that regulates the transcription of emerin and many other muscle-relevant genes. *Hum. Mol. Genet.* **15**, 3459–3472 (2006).

44. Ooshio, T. et al. Involvement of LMO7 in the association of two cell-cell adhesion molecules, nectin and E-cadherin, through afadin and α-actinin in epithelial cells. *J. Biol. Chem.* **279**, 31365–31373 (2004).

45. Liu, C. X., Li, Y., Obermoeller-McCormick, L. M., Schwartz, A. L. & Bu, G. The putative tumor suppressor LRP1B, a novel member of the low density lipoprotein (LDL) receptor family, exhibits both overlapping and distinct properties with the LDL receptor-related protein. *J. Biol. Chem.* **276**, 28889–28896 (2001).

46. Hirt, M. N. et al. Functional improvement and maturation of rat and human engineered heart tissue by chronic electrical stimulation. *J. Mol. Cell. Cardiol.* **74**, 151–161 (2014).

47. Neufing, P. J. et al. Exposure and binding of selected immunodominant La/SSB epitopes on human apoptotic cells. *Arthritis Rheum.* **52**, 3934–3942 (2005).

48. Zhou, B. & Tian, R. Mitochondrial dysfunction in pathophysiology of heart failure. *J. Clin. Invest.* **128**, 3716–3726 (2018).

49. Chen, Y. R. & Zweier, J. L. Cardiac mitochondria and reactive oxygen species generation. *Circ. Res.* **114**, 524–537 (2014).

50. Nomura, S. et al. Cardiomyocyte gene programs encoding morphological and functional signatures in cardiac hypertrophy and failure. *Nat. Commun.* **9**, 4435 (2018).

51. Izmirly, P., Saxena, A. & Buyon, J. P. Progress in the pathogenesis and treatment of cardiac manifestations of neonatal lupus. *Curr. Opin. Rheumatol.* **29**, 467–472 (2017).

52. Seki, M. et al. Acute and chronic increases of circulating FSTL1 normalize energy substrate metabolism in pacing-induced heart failure. *Circ. Heart Fail.* **11**, e004486 (2018).

53. Mattiotti, A., Prakash, S., Barnett, P. & van den Hoff, M. J. B. Follistatin-like 1 in development and human diseases. *Cell Mol. Life Sci.* **75**, 2339–2354 (2018).

54. Tanaka, K. et al. Follistatin-like 1 regulates hypertrophy in heart failure with preserved ejection fraction. *JACC Basic Transl. Sci.* **1**, 207–221 (2016).

55. Wei, K. et al. Epicardial FSTL1 reconstitution regenerates the adult mammalian heart. *Nature* **525**, 479–485 (2015).

56. Oshima, Y. et al. Follistatin-like 1 is an Akt-regulated cardioprotective factor that is secreted by the heart. *Circulation* **117**, 3099–3108 (2008).

57. Xie, Y. et al. LMO7 is a negative feedback regulator of transforming growth factor β signaling and fibrosis. *Circulation* **139**, 679–693 (2019).

58. Lopez-Guisa, J. M. et al. Mannose receptor 2 attenuates renal fibrosis. *J. Am. Soc. Nephrol.* **23**, 236–251 (2012).

59. Biagioni, A. et al. uPAR knockout results in a deep glycolytic and OXPHOS reprogramming in melanoma and colon carcinoma cell lines. *Cells* **9**, 308 (2020).

60. Kotipatruni, R. R. et al. Apoptosis induced by knockdown of uPAR and MMP-9 is mediated by inactivation of EGFR/STAT3 signaling in medulloblastoma. *PLoS ONE* **7**, e44798 (2012).

61. Alfano, D., Franco, P. & Stoppelli, M. P. Modulation of cellular function by the urokinase receptor signalling: a mechanistic view. *Front. Cell Dev. Biol.* **10**, 818616 (2022).

62. Gladman, D. D., Ibanez, D. & Urowitz, M. B. Systemic lupus erythematosus disease activity index 2000. *J. Rheumatol.* **29**, 288–291 (2002).

63. Huebsch, N. et al. Automated video-based analysis of contractility and calcium flux in human-induced pluripotent stem cell-derived cardiomyocytes cultured over different spatial scales. *Tissue Eng. Part C Methods* **21**, 467–479 (2015).

64. Chen, T. W. et al. Ultrasensitive fluorescent proteins for imaging neuronal activity. *Nature* **499**, 295–300 (2013).

65. Hayashi, Y. et al. BMP-SMAD-ID promotes reprogramming to pluripotency by inhibiting p16/INK4A-dependent senescence. *Proc. Natl Acad. Sci. USA* **113**, 13057–13062 (2016).

66. Burridge, P. W. et al. Chemically defined generation of human cardiomyocytes. *Nat. Methods* **11**, 855–860 (2014).

67. Bray, N. L., Pimentel, H., Melsted, P. & Pachter, L. Near-optimal probabilistic RNA-seq quantification. *Nat. Biotechnol.* **34**, 525–527 (2016).

68. Torgerson, W. S. Multidimensional scaling, I: theory and method. *Psychometrika* **17**, 401–419 (1952).

69. Jolliffe, I.T. *Principal Component Analysis* (Springer, 2002).

70. Everitt, B.S., Landau, S. & Leese, M. *Cluster Analysis* (Wiley, 2011).

71. Robinson, M. D. & Oshlack, A. A scaling normalization method for differential expression analysis of RNA-seq data. *Genome Biol.* **11**, R25 (2010).

72. Ritchie, M. E. et al. limma powers differential expression analyses for RNA-sequencing and microarray studies. *Nucleic Acids Res.* **43**, e47 (2015).

73. Law, C. W., Chen, Y., Shi, W. & Smyth, G. K. voom: precision weights unlock linear model analysis tools for RNA-seq read counts. *Genome Biol.* **15**, R29 (2014).

74. Liu, R. et al. Why weight? Modelling sample and observational level variability improves power in RNA-seq analyses. *Nucleic Acids Res.* **43**, e97 (2015).

75. Smyth, G. K., Michaud, J. & Scott, H. S. Use of within-array replicate spots for assessing differential expression in microarray experiments. *Bioinformatics* **21**, 2067–2075 (2005).

76. Kanehisa, M., Goto, S., Kawashima, S., Okuno, Y. & Hattori, M. The KEGG resource for deciphering the genome. *Nucleic Acids Res.* **32**, D277–D280 (2004).

77. Ashburner, M. et al. Gene Ontology: tool for the unification of biology. *Nat. Genet.* **25**, 25–29 (2000).

78. Ahsan, S. & Draghici, S. Identifying significantly impacted pathways and putative mechanisms with iPathwayGuide. *Curr. Protoc. Bioinformatics* **57**, 7.15.11–17.15.30 (2017).

79. Draghici, S. et al. A systems biology approach for pathway level analysis. *Genome Res.* **17**, 1537–1545 (2007).

80. Tarca, A. L. et al. A novel signaling pathway impact analysis. *Bioinformatics* **25**, 75–82 (2009).

81. Alexa, A., Rahnenfuhrer, J. & Lengauer, T. Improved scoring of functional groups from gene expression data by decorrelating GO graph structure. *Bioinformatics* **22**, 1600–1607 (2006).

82. Meier, F. et al. diaPASEF: parallel accumulation-serial fragmentation combined with data-independent acquisition. *Nat. Methods* **17**, 1229–1236 (2020).

83. Hughes, C. S. et al. Single-pot, solid-phase-enhanced sample preparation for proteomics experiments. *Nat. Protoc.* **14**, 68–85 (2019).

84. Demichev, V., Messner, C. B., Vernardis, S. I., Lilley, K. S. & Ralser, M. DIA-NN: neural networks and interference correction enable deep proteome coverage in high throughput. *Nat. Methods* **17**, 41–44 (2020).

85. Tyanova, S. et al. The Perseus computational platform for comprehensive analysis of (prote)omics data. *Nat. Methods* **13**, 731–740 (2016).

86. Uhlen, M. et al. Proteomics. Tissue-based map of the human proteome. *Science* **347**, 1260419 (2015).

87. Binder, J. X. et al. COMPARTMENTS: unification and visualization of protein subcellular localization evidence. *Database (Oxford)* **2014**, bau012 (2014).

88. Luecke, L. B. et al. Surfaceome mapping of primary human heart cells with CellSurfer uncovers cardiomyocyte surface protein LSMEM2 and proteome dynamics in failing hearts. *Nat. Cardiovasc. Res.* **2**, 76–95 (2023).

89. Mohan, D. et al. PhIP-Seq characterization of serum antibodies using oligonucleotide-encoded peptidomes. *Nat. Protoc.* **13**, 1958–1978 (2018).

## Acknowledgements

## Author contributions

S.F., T.R.N., M.A.T., L.G.-P., R.W. and G.V.-N. devised the study and designed the experiments. S.F., T.R.N., M.A.T., R.I.L., G.V., P.L.G., V.L., M.J.L., M.L., R.Z.Z. and J.W. performed experiments. S.F., T.R.N., M.A.T., R.I.L., G.V., P.L.G., V.L., D.N.T., Y.K., R.A.F. and R.K.S. analyzed data. S.F., T.R.N., M.A.T., G.V., R.A.F., J.G.S., C.E.S., L.G.-P., R.W. and G.V.-N interpreted data and provided input. S.F., T.R.N., R.W. and G.V.-N. wrote the manuscript.

## Competing interests

The authors declare no competing interests.

## Additional information

**Extended data** is available for this paper at https://doi.org/10.1038/s44161-024-00525-w.

**Supplementary information** The online version contains supplementary material available at https://doi.org/10.1038/s44161-024-00525-w.

**Correspondence and requests for materials** should be addressed to Gordana Vunjak-Novakovic.

**Peer review information** *Nature Cardiovascular Research* thanks Sean Wu, Madeleine Cunningham, Hal Scofield and the other, anonymous, reviewer(s) for their contribution to the peer review of this work.

[1]Department of Biomedical Engineering, Columbia University, New York, NY, USA. [2]Department of Genetics, Harvard Medical School, Boston, MA, USA.
[3]Biomedical Informatics Shared Resource, Herbert Irving Comprehensive Cancer Center, Columbia University, New York, NY, USA. [4]Department of
Biomedical Informatics, Columbia University, New York, NY, USA. [5]Proteomics and Macromolecular Crystallography Shared Resource, Herbert Irving
Comprehensive Cancer Center, Columbia University, New York, NY, USA. [6]Division of Cardiovascular Medicine, Brigham and Women's Hospital & Harvard
Medical School, Boston, MA, USA. [7]Howard Hughes Medical Institute, Chevy Chase, MD, USA. [8]Department of Medicine, Columbia University,
New York, NY, USA. [9]Columbia Center for Translational Immunology, Columbia University College of Physicians and Surgeons, New York, NY, USA.
[10]College of Dental Medicine, Columbia University, New York, NY, USA. [11]These authors contributed equally: Sharon Fleischer, Trevor R. Nash.
✉e-mail: gv2131@columbia.edu
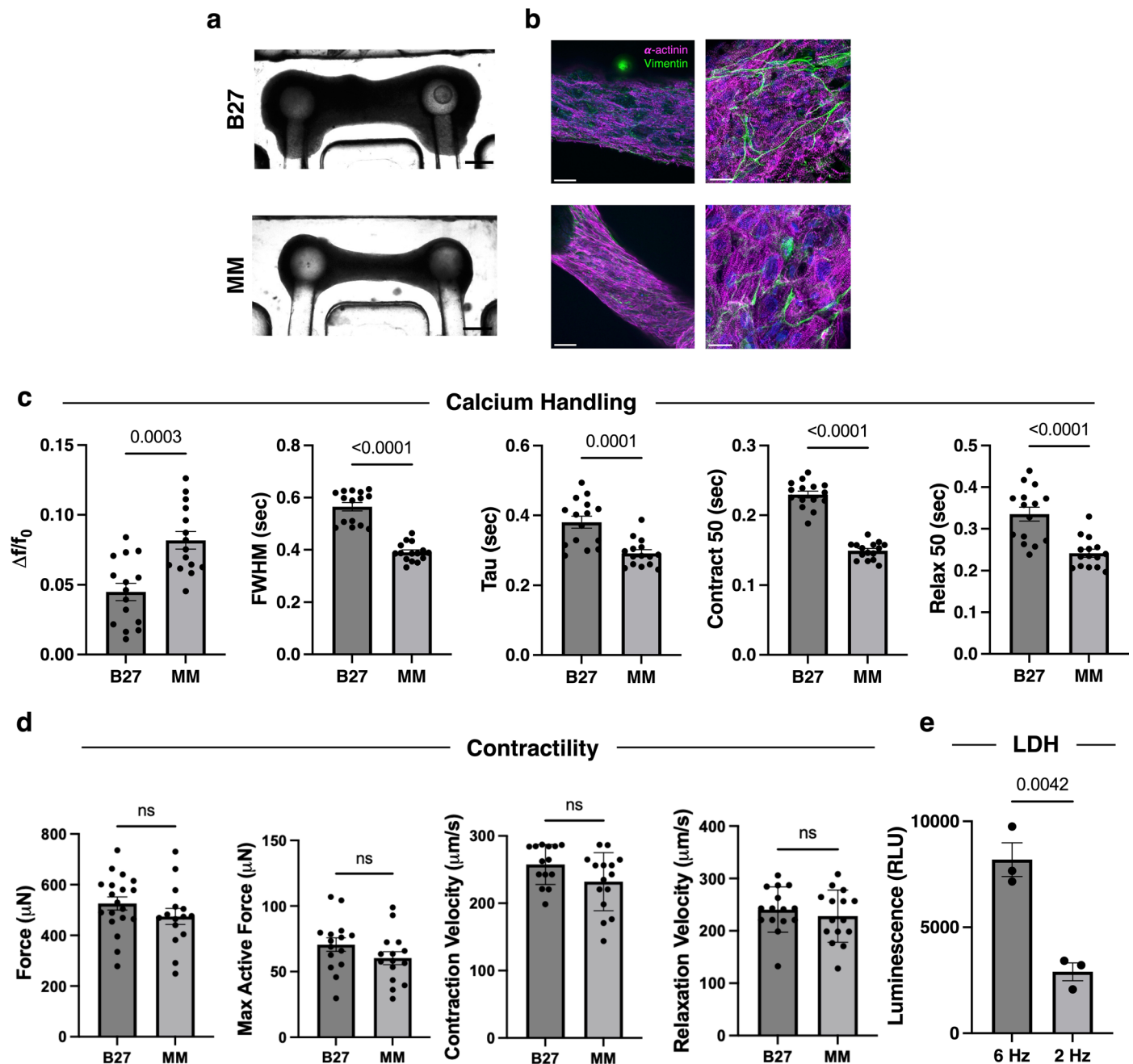
**Extended Data Fig. 1 | Characterization of electromechanically stimulated engineered cardiac tissues cultured in different media formulations.**
(**a, b**) Representative brightfield (**a**) and immunofluorescence (**b**) images of engineered cardiac tissues cultured in standard RPMI-B27 (B27) medium (top) and metabolic maturation (MM) medium (bottom). (**c, d**) Measurements of calcium handling (**c**) and contractility (**d**) of engineered cardiac tissues cultured in B27 medium and MM. n = 15 cardiac tissue per group. (**e**) Quantification of LDH release into supernatant from engineered cardiac tissues during electrical stimulation at 2 Hz and 6 Hz. n = 3 cardiac tissues per group. Statistical significance was determined using unpaired two-tailed Student's t-test. Data represented as mean ± s.e.m. Individual values are indicated by dots. B27, RPMI-1640 with B27 supplement. MM, metabolic maturation medium. LDH, lactate dehydrogenase. Scale bars in (**a**) are 500 μm; scale bars in (**b**) are 200 μm (left) and 10 μm (right). n.s., not significant.
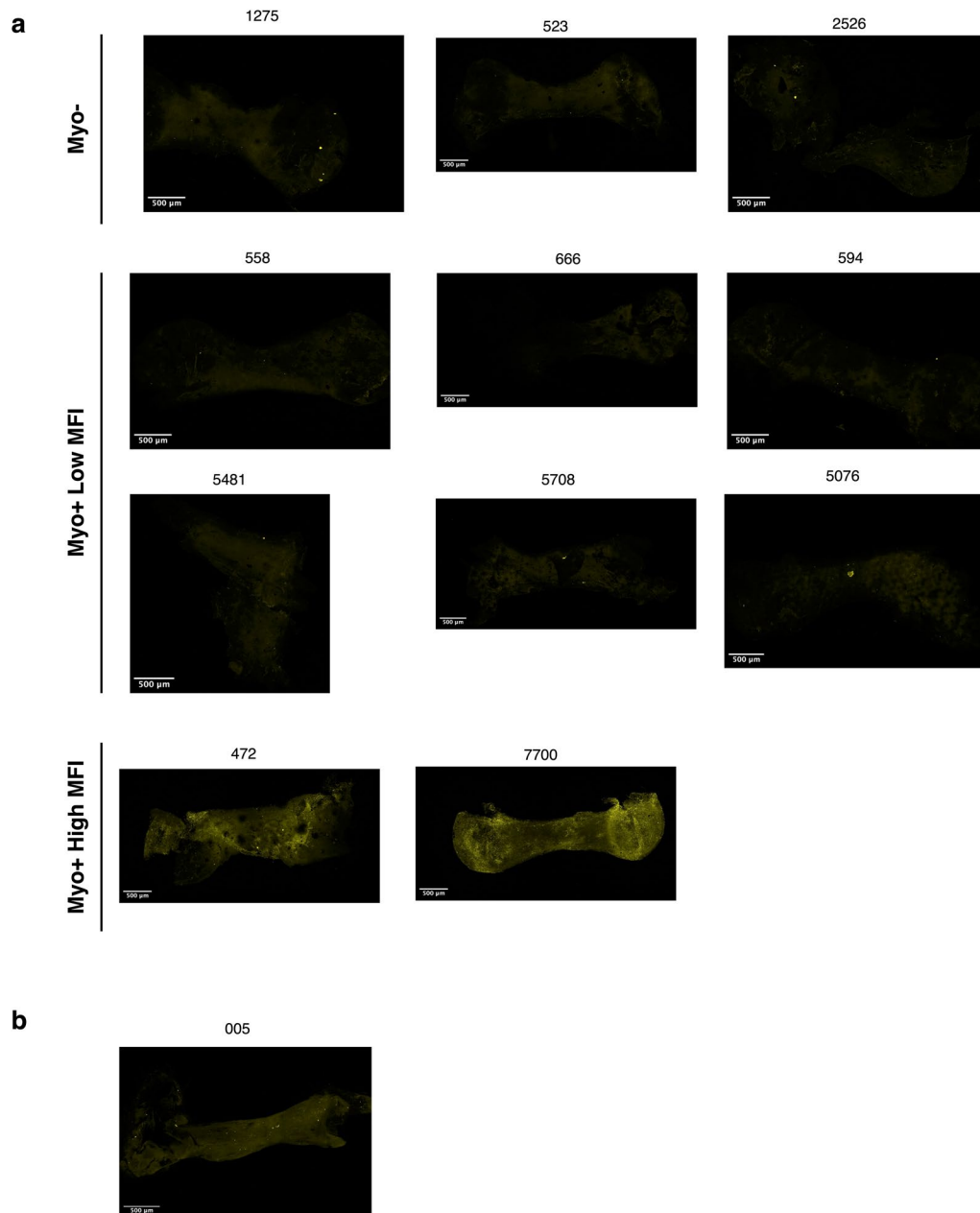
**Extended Data Fig. 2 | Immunostaining of patient IgG binding to engineered cardiac tissues.** (**a**) Immunofluorescence images of engineered cardiac tissues treated with IgG isolated from each patient in the Myo- and Myo+ groups, followed by fixation and staining with anti-human IgG to visualize patient-specific IgG binding (yellow). Patient samples from the Myo+ group are subclassified as low MFI and high MFI based on quantification of human IgG staining in engineered cardiac tissues. (**b**) Immunofluorescence image of engineered cardiac tissues cultured with IgG isolated from an additional Myo+ SLE patient with elevated levels of myocardial inflammation (SUVmax = 12.4) and stained with secondary anti-human IgG.
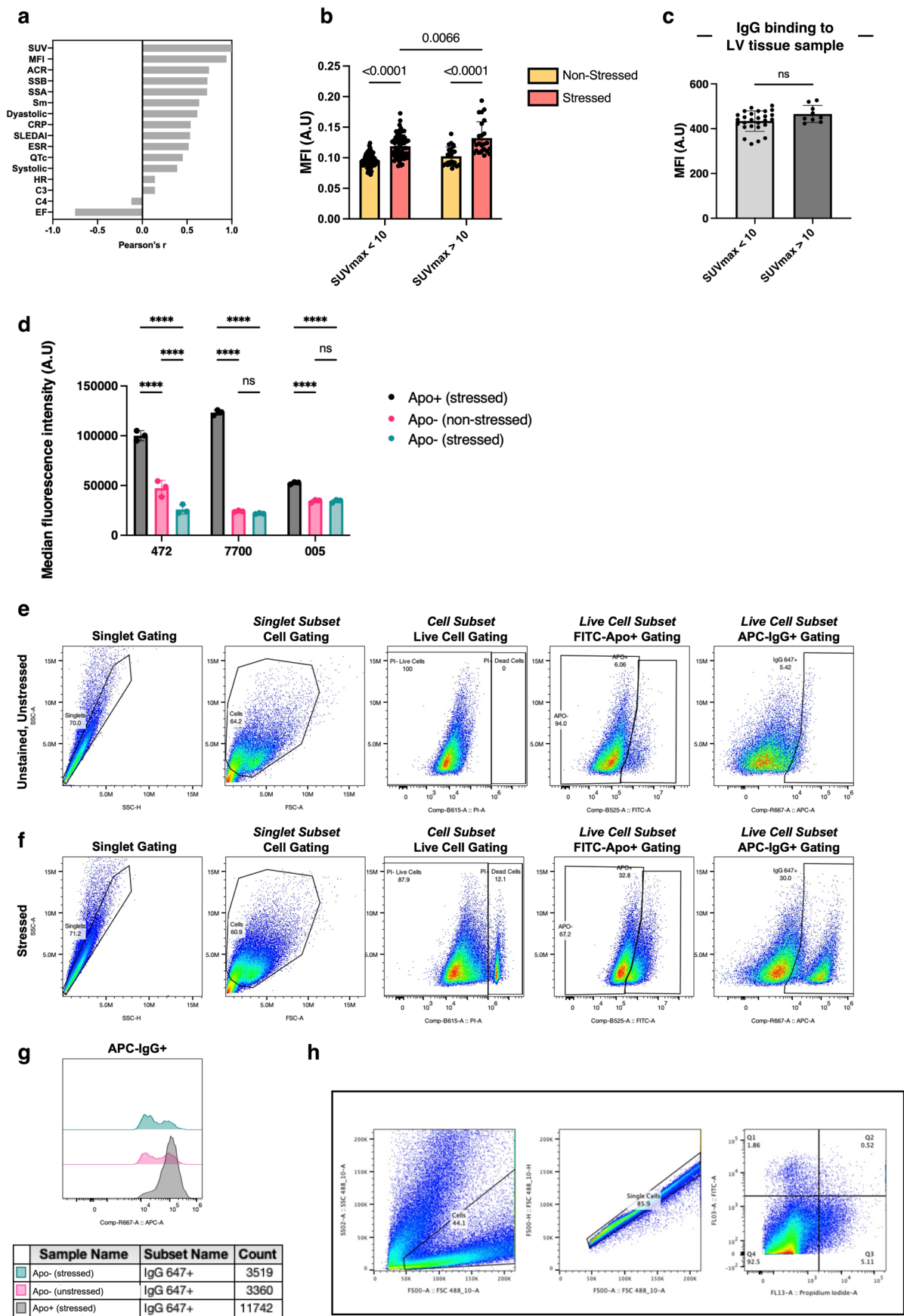
**Extended Data Fig. 3 | See next page for caption.**

**Extended Data Fig. 3 | Quantitative analysis of IgG binding to cardiac tissues and individual cells. (a)** Summary of Pearson correlation coefficients of clinical 18F-FDG uptake quantified as SUVs compared with corresponding patient IgG binding levels to engineered tissues in vitro (MFI, second row) and with other clinical data collected as part of the cohort. **(b,c)** IgG binding level quantification (measured by MFI) of IgG isolated from patients with low levels of myocardial inflammation (SUVmax < 10) and elevated myocardial inflammation (SUVmax > 10) to stressed and non-stressed hiPSC-cardiomyocytes **(b)** and healthy left ventricle (LV) tissue sample **(c)**. n = 9 patients with SUVmax < 10, and n = 3 patients with SUVmax > 10; n = 8 fields of view per patient in **(b)** or n = 3 fields of view per patient in **(c)**. **(d)** Flow analysis of IgG binding to live and apoptotic hiPSC-CMs (Apo + ), and live, non-apoptotic (Apo-) stressed and non-stressed

hiPSC-CMs in the three cohort patients with elevated myocardial inflammation. n = 3 biological replicates per patient. **(e-g)** Sample gating strategy of Apotracker Green+ and IgG+ in stressed and non-stressed iPSC-CMs. Pseudocolor scatter plots of **(e)** unstained, unstressed hiPSC-CMs and **(f)** stressed hiPSC-CMs stained for Propidium Iodide (PI), Apotracker, and Alexa Fluor 647-conjugated anti-human IgG. **(g)** Histogram of IgG binding in stressed Apotacker+ (black), non-stressed Apotracker- (pink), or stressed Apotracker- (teal) hiPSC-CMs. **(h)** Example flow cytometry gating strategy used to identify live (PI-, Apotracker green-) hiPSC-CMs, shown in Q4. Data represented as mean ± s.e.m. Ordinary two-way ANOVA with Tukey's test for multiple comparisons in **(b,d)** and unpaired two-tailed Student's t-test in **(c)**. **** p < 0.0001.
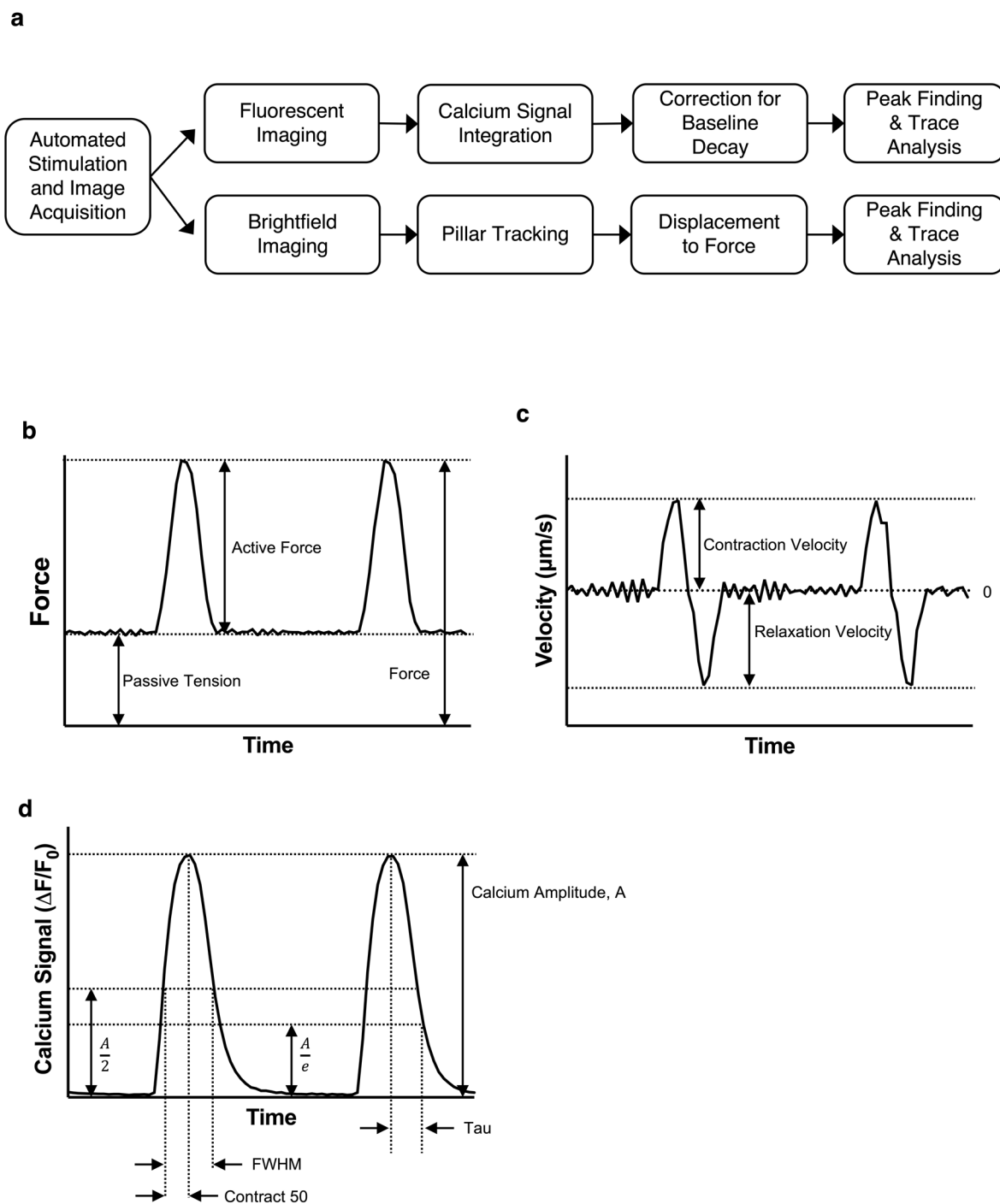
**Extended Data Fig. 4 | Functional analysis of engineered cardiac tissue.** (**a**) Schematic overview of the automated imaging and analysis pipeline for characterizing engineered cardiac tissue function. (**b-d**) Representative traces of engineered cardiac tissue force generation (**b**), velocity (**c**), and calcium signal (**d**). Metrics used to quantify these traces are depicted on each plot.
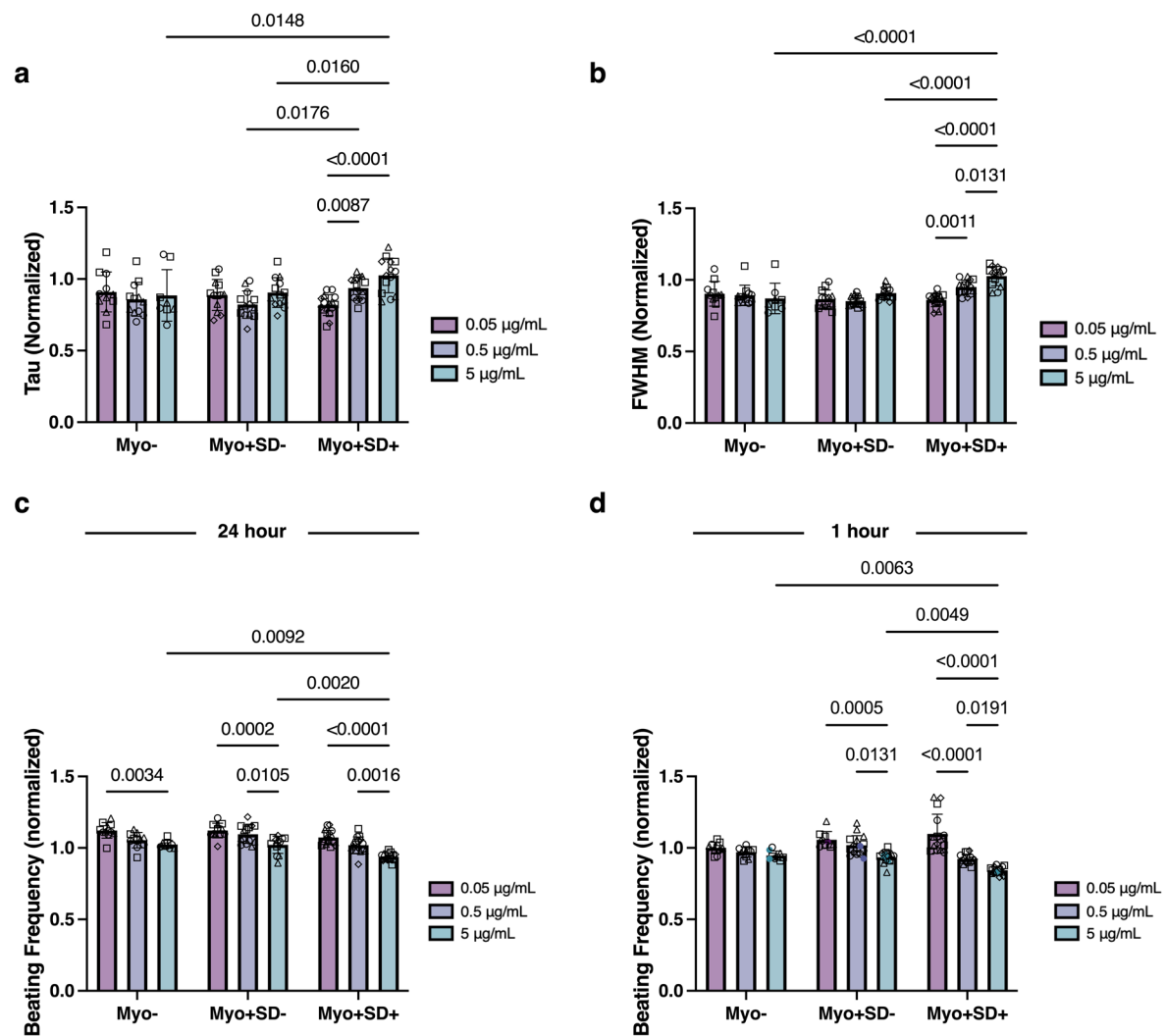
**Extended Data Fig. 5 | Dose-response effect of patient IgG on hiPSC-cardiomyocyte calcium handling and beating frequency. (a,b)** IgG from Myo+SD+ patients demonstrate a clear dose-response effect in hiPSC-derived cardiomyocytes calcium handling measurements of tau (**a**) and FWHM (**b**). (**c,d**) Beating 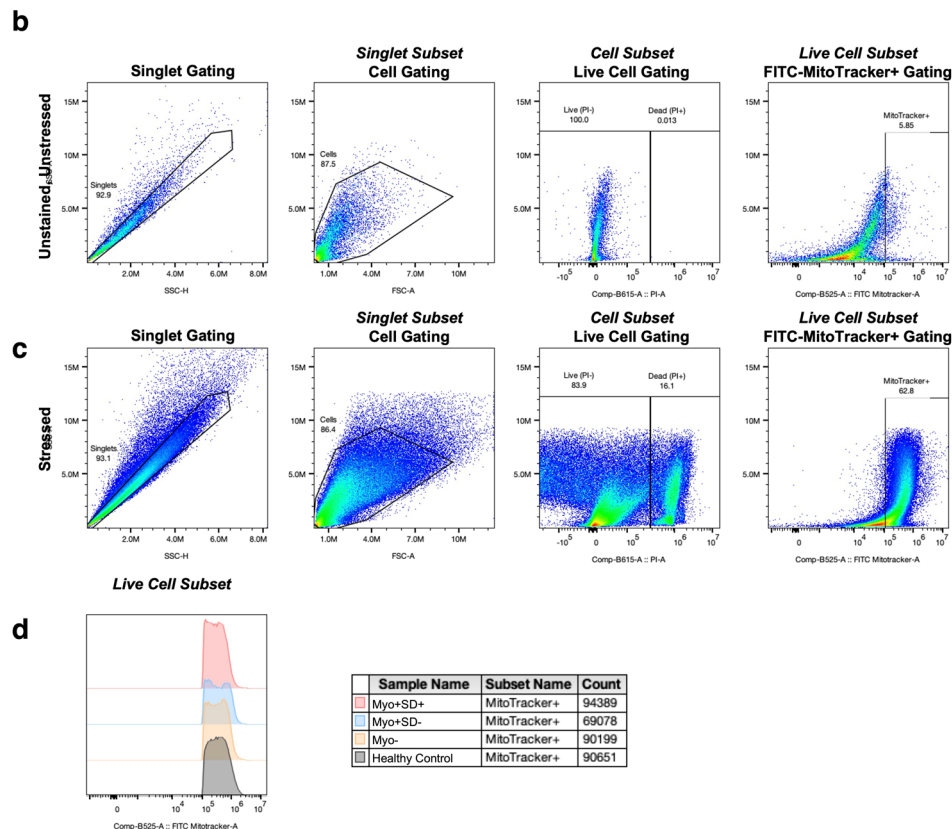frequency measurements of hiPSC-CMs imaged 24 hours (**c**) and 1 hour (**d**) after the addition of patient IgG. Data represented as mean ± s.e.m. n = 3 Myo- patients, n = 4 Myo+SD- patients, and n = 4 Myo+SD+ patients; n = 4 wells per patient. Symbol shapes represent different patients within each group. Statistical significance was determined by ordinary two-way ANOVA with Tukey's test for multiple comparisons.
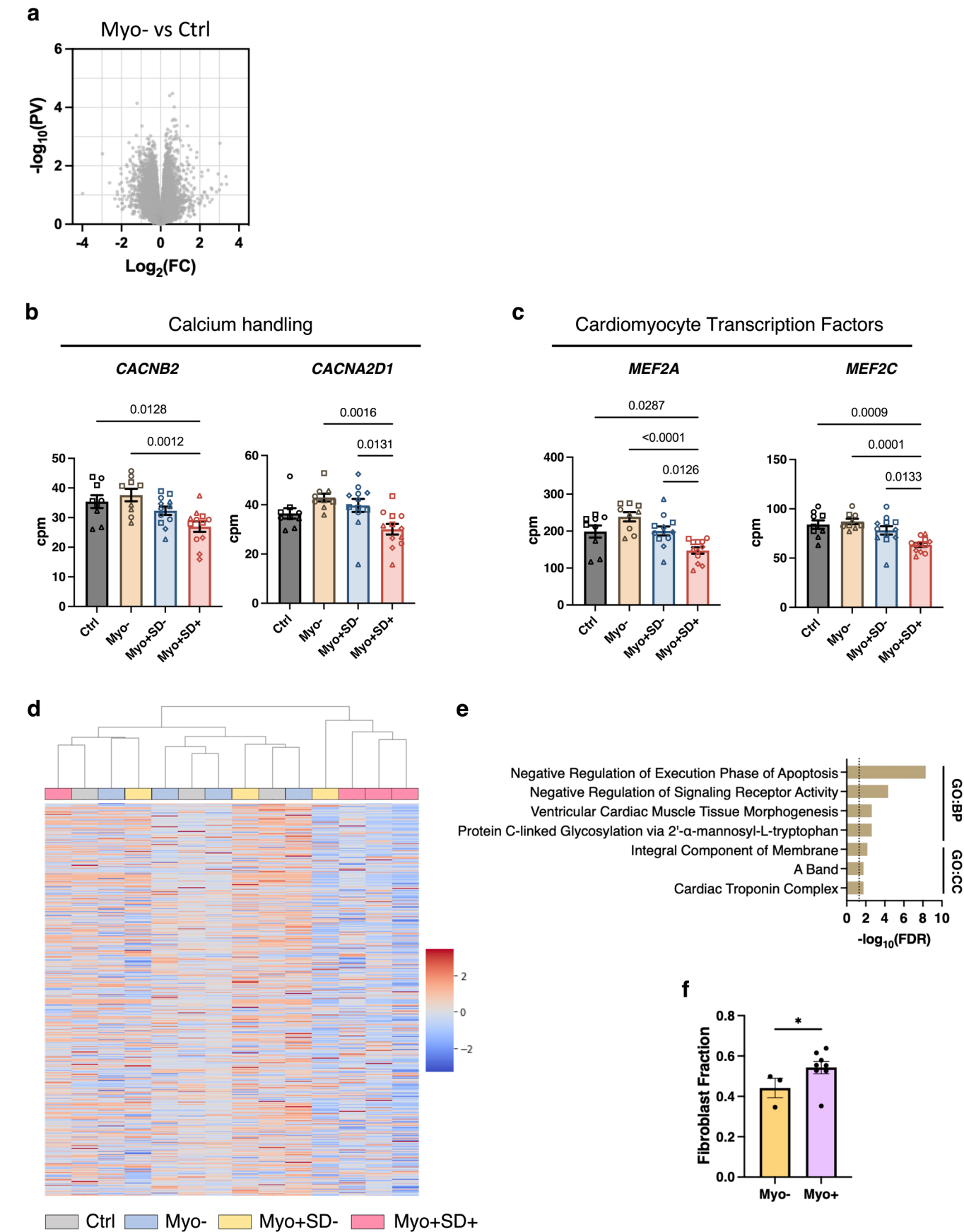
**Extended Data Fig. 6 | See next page for caption.**

**Extended Data Fig. 6 | Transcriptomics of engineered cardiac tissues treated with patient IgG.** (**a**) Volcano plot of DEGs between engineered cardiac tissues treated with Myo- patient IgG and those treated with healthy control patient IgG (n = 3 individuals per group, n = 3 tissues per individual). Statistical significance was determined by two-sided Student's t-test with Benjamini-Hochberg correction for multiple comparisons. (**b,c**) Expression of genes related to calcium handling (**b**), and cardiomyocyte transcription factors (**c**) in tissues cultured with IgG from healthy controls and SLE patient subgroups; n = 3 Myo- patients, n = 4 Myo+SD- patients, and n = 4 Myo+SD+ patients; n = 3 tissues per patient. Ordinary one-way ANOVA with Tukey's test for multiple comparisons. (**d**) Hierarchical clustering of overall transcriptomics of engineered cardiac tissues treated with IgG from each individual patient. Each column represents the average expression of n = 3 independent tissues treated with IgG from the same patient. (**e**) GO biological processes (GO:BP), and GO cellular compartment (GO:CC) pathway analysis of DEGs between tissue cultured with IgG from Myo+SD+ and Myo+SD- patient groups. (**f**) Fibroblasts fraction in engineered cardiac tissues assessed with CIBERSORTx. Individual points represent the average of n = 3 tissues per patient. Statistical analysis was performed using Mann–Whitney U-test. Data represented as mean ± s.e.m. Symbol shapes represent different patients within each group.

**a**



**b**



**c**



**d**



| | Sample Name | Subset Name | Count |
|---|---|---|---|
| | Myo+SD+ | MitoTracker+ | 94389 |
| | Myo+SD- | MitoTracker+ | 69078 |
| | Myo- | MitoTracker+ | 90199 |
| | Healthy Control | MitoTracker+ | 90651 |

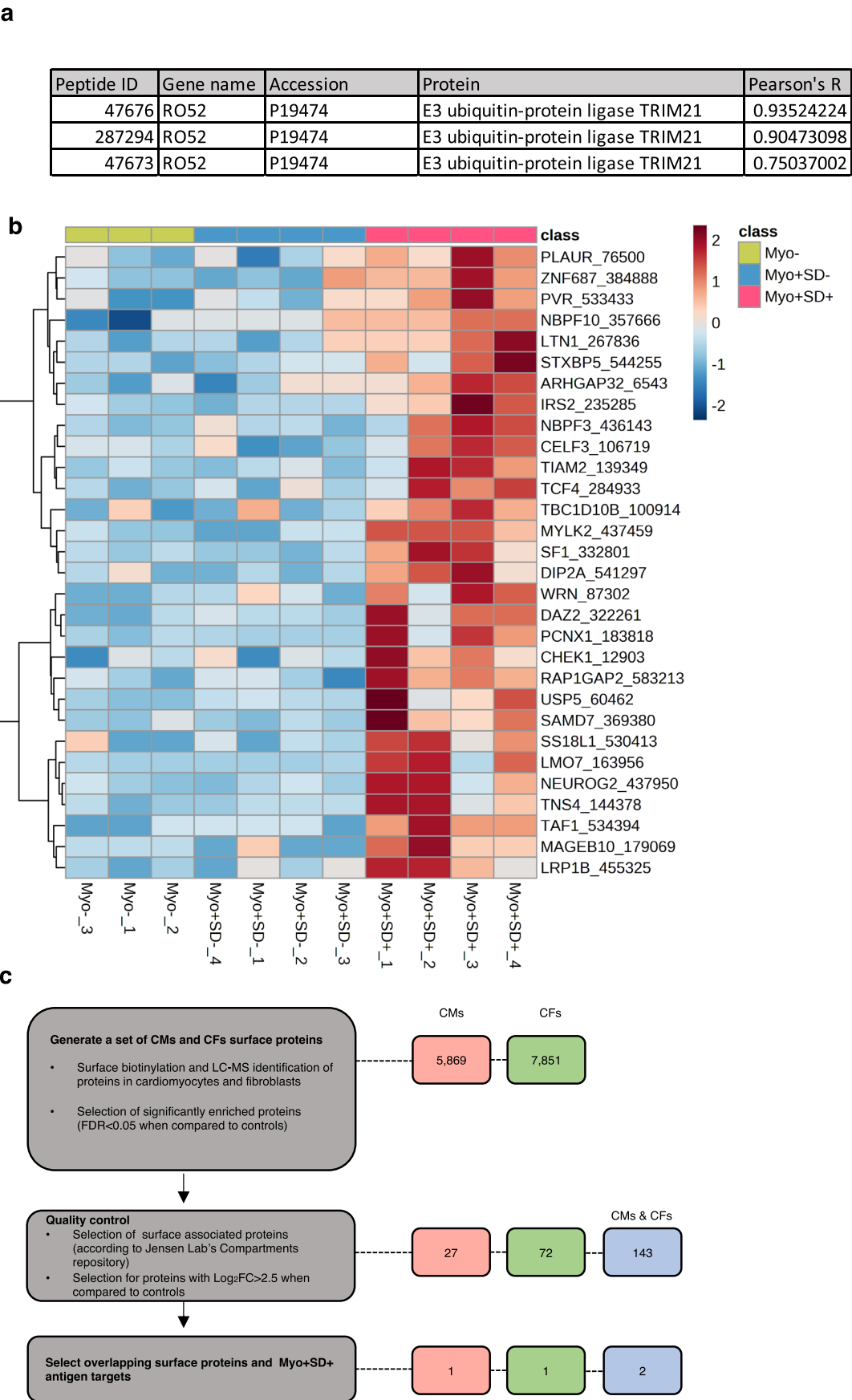**Extended Data Fig. 7 | See next page for caption.**

**Extended Data Fig. 7 | Myo+SD+ IgG alter cardiomyocyte respiration.**
(**a**) Schematic of the effects of Myo+SD+ IgG on oxidative phosphorylation pathway in cardiomyocytes. Red and blue boxes indicate upregulated and downregulated genes in the cardiomyocyte population, respectively, in tissues cultured with Myo+SD+ IgG compared to tissues cultured with Myo- IgG. (**b-c**) Sample gating of MitoTracker Green+ hiPSC-CMs cultured with patient IgG. Pseudocolor scatter plots of (**b**) unstained hiPSC-CMs and (**c**) hiPSC-CMs cultured with IgG from Myo+SD+ patients and stained for Propidium Iodide (PI) and MitoTracker Green. (**d**) Histogram of MitoTracker+ hiPSC-CMs cultured with IgG from healthy (black), Myo- (orange), Myo+SD- (blue), or Myo+SD+ (red) patients. hiPSC-CMs were dissociated prior to staining and analysis.
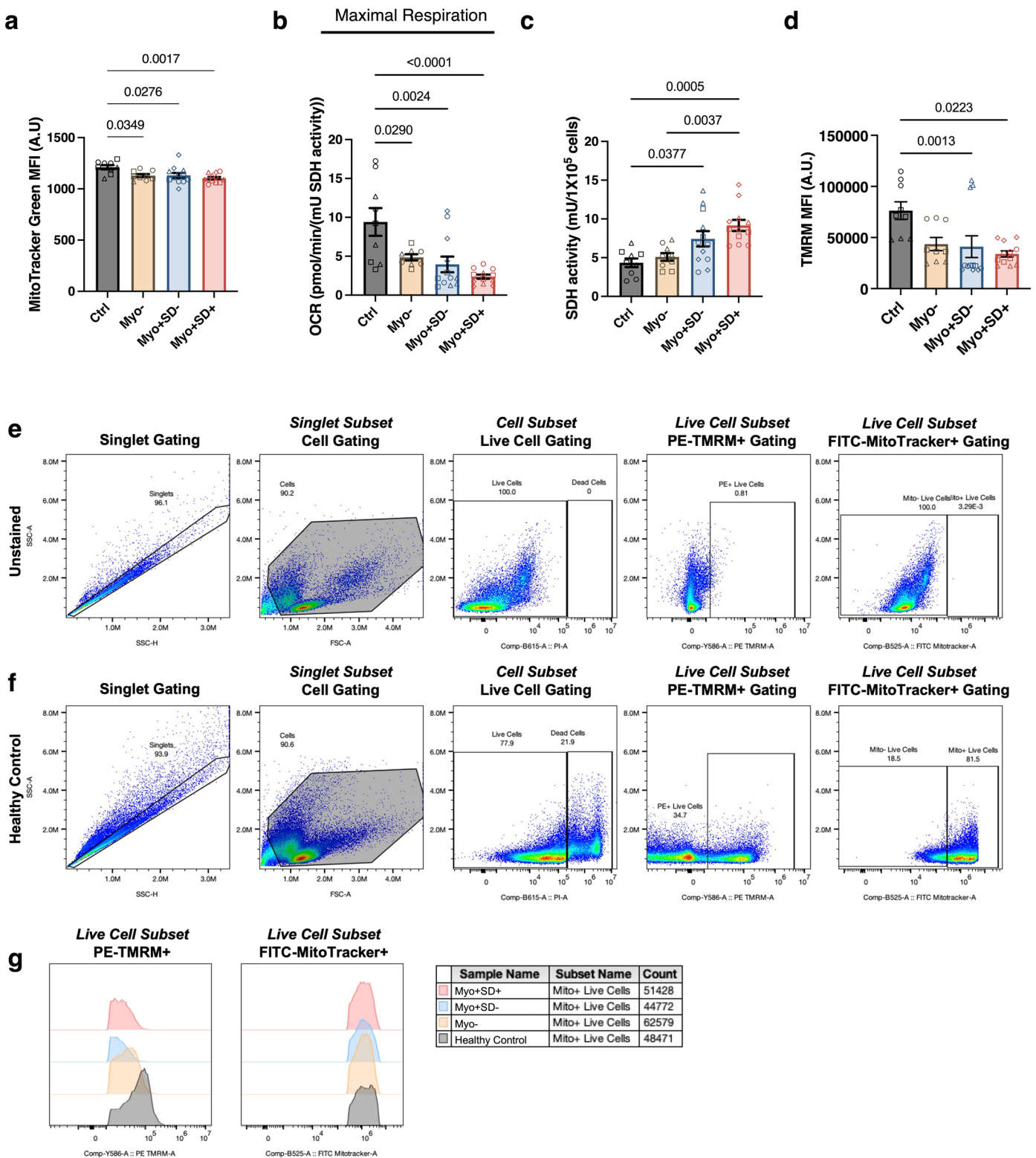
**Extended Data Fig. 8 | IgGs from Myo+SD+ patients reduce mitochondrial content, respiration and respiratory efficiency in PBMCs.** (a-d) Changes in mitochondrial quantity (**a**), maximal respiration (**b**), SDH activity (**c**) and mitochondrial membrane potential (**d**), in PBMCs treated with SLE patient and healthy control IgG; n = 3 healthy controls, n = 3 Myo- patients, n = 4 Myo+SD- patients, and n = 4 Myo+SD+ patients; n = 3 wells per patient. Symbol shapes represent different patients within each group. Data represented as mean ± s.e.m.

Ordinary one-way ANOVA with Tukey's test for multiple comparisons in a,c,d, ordinary one-way ANOVA with Dunn's post-hoc comparisons test in b. (**e-g**) Sample gating of TMRM+ and MitoTracker Green+ human PBMCs cultured with patient IgG. Pseudocolor scatter plots of (**e**) unstained PBMCs and (**f**) PBMCs stained for Propidium Iodide (PI), TMRM, and MitoTracker Green. (**g**) Histograms of TMRM+ and MitoTracker+ PBMCs cultured with IgG from healthy (black), Myo- (orange), Myo+SD- (blue), or Myo+SD+ (red) patients.

**a**

| Peptide ID | Gene name | Accession | Protein | Pearson's R |
|---|---|---|---|---|
| 47676 | RO52 | P19474 | E3 ubiquitin-protein ligase TRIM21 | 0.93524224 |
| 287294 | RO52 | P19474 | E3 ubiquitin-protein ligase TRIM21 | 0.90473098 |
| 47673 | RO52 | P19474 | E3 ubiquitin-protein ligase TRIM21 | 0.75037002 |

**b**



**c**



**Extended Data Fig. 9 | PhIP-Seq analysis of patient-specific antigen targets.**
(**a**) Table summarizing Pearson's R quantified by correlation between different RO52 peptides measured by PhIP-Seq and clinical laboratory measurements of patient anti-Ro/SSA antibodies by ELISA. (**b**) Hierarchical clustering of peptides increased in Myo+SD+ patients compared to Myo- and Myo+SD- patients. Each column represents a patient (green; Myo- patients, blue; Myo+SD+ patients pink; Myo+SD+ patients). Each row represents a peptide identified by PhIP-Seq. (**c**) Schematic of surface protein analysis pipeline and filtering of identified proteins.

**Extended Data Table 1 | Clinical data of an additional patient with SLE with elevated levels of myocardial inflammation (SUVmax=12.4)**

| Group | Myocardial Inflammation (+) |
|---|---|
| Study ID | 005 |
| Age | 32 |
| Sex | Female |
| Level of Care | Inpatient |
| Disease Duration (years) | 0.5 |
| FDG-Uptake (max SUV) | 12.4 |
| EF (%) | 55-60 |
| QTc (ms) | 449 |
| Troponin (ng/mL) | <0.01 |
| ACR Criteria | N/A |
| SLEDAI | 4 |
| ESR (mm/hr) | N/A |
| CRP (mg/L) | 72 |
| C3 (mg/dL) | 117 |
| C4 (mg/dL) | 17 |
| anti-dsDNA Antibody (IU) | <6 |
| SSA Antibody (AI) | Positive |
| SSB Antibody (AI) | <0.2 |
| Smith Antibody (AI) | <0.2 |
| B2GP IgG (SGU) | 0 |
| B2GP IgM (SMU) | 0 |
| ACL IgG (GPL) | 0 |
| ACL IgM (MPL) | 0 |
| HbA1c (%) | N/A |
| Systolic BP (mm Hg) | N/A |
| Diastolic BP (mm Hg) | N/A |
| BMI (kg/m$^2$) | N/A |
| Total Cholesterol (mg/dL) | N/A |
| Triglycerides (mg/dL) | N/A |
| HDL (mg/dL) | N/A |
| LDL (mg/dL) | N/A |

# nature portfolio

Corresponding author(s): Gordana Vunjak-Novakovic

Last updated by author(s): Jul 15, 2024

# Reporting Summary

Nature Portfolio wishes to improve the reproducibility of the work that we publish. This form provides structure for consistency and transparency in reporting. For further information on Nature Portfolio policies, see our Editorial Policies and the Editorial Policy Checklist.

## Statistics

For all statistical analyses, confirm that the following items are present in the figure legend, table legend, main text, or Methods section.

| n/a | Confirmed | |
|---|---|---|
| ☐ | ☒ | The exact sample size (*n*) for each experimental group/condition, given as a discrete number and unit of measurement |
| ☐ | ☒ | A statement on whether measurements were taken from distinct samples or whether the same sample was measured repeatedly |
| ☐ | ☒ | The statistical test(s) used AND whether they are one- or two-sided<br>*Only common tests should be described solely by name; describe more complex techniques in the Methods section.* |
| ☒ | ☐ | A description of all covariates tested |
| ☐ | ☒ | A description of any assumptions or corrections, such as tests of normality and adjustment for multiple comparisons |
| ☐ | ☒ | A full description of the statistical parameters including central tendency (e.g. means) or other basic estimates (e.g. regression coefficient) AND variation (e.g. standard deviation) or associated estimates of uncertainty (e.g. confidence intervals) |
| ☐ | ☒ | For null hypothesis testing, the test statistic (e.g. *F*, *t*, *r*) with confidence intervals, effect sizes, degrees of freedom and *P* value noted<br>*Give P values as exact values whenever suitable.* |
| ☒ | ☐ | For Bayesian analysis, information on the choice of priors and Markov chain Monte Carlo settings |
| ☒ | ☐ | For hierarchical and complex designs, identification of the appropriate level for tests and full reporting of outcomes |
| ☐ | ☒ | Estimates of effect sizes (e.g. Cohen's *d*, Pearson's *r*), indicating how they were calculated |

*Our web collection on statistics for biologists contains articles on many of the points above.*

## Software and code

Policy information about availability of computer code

| | |
|---|---|
| Data collection | Functional data for engineered tissues were collected using previously published code from our lab [ref28] |
| Data analysis | All software used to analyze the data is commercial or open-source. Functional data for engineered tissues were analyzed using previously published code from our lab [ref. 28]. LC-MS/MS data were analyzed with Perseus v2.0.3.1. Statistics were analyzed using GraphPad Prism v10.0. Image data analysis was performed using the FIJI distribution of ImageJ. RNA-seq reads were quantified with the kallisto package and differential expression analysis was conducted with the limma R package (v3.55.0). Pathway analysis was performed with iPathwayGuide. Bio-Rad Everest Software was used to collect data, and FlowJo 10.10 was used for data analysis. |

For manuscripts utilizing custom algorithms or software that are central to the research but not yet described in published literature, software must be made available to editors and reviewers. We strongly encourage code deposition in a community repository (e.g. GitHub). See the Nature Portfolio guidelines for submitting code & software for further information.

# Data

All manuscripts must include a data availability statement. This statement should provide the following information, where applicable:

- Accession codes, unique identifiers, or web links for publicly available datasets
- A description of any restrictions on data availability
- For clinical datasets or third party data, please ensure that the statement adheres to our policy

> All data are available in the main manuscript, extended data, or associated Figshare site. All raw sequencing data are deposited at NCBI Gene Expression Omnibus (GEO), accession number: GSE227571. Previously published datasets used in this study include: UniProt Human proteome database (UP000005640), and Human Cell Atlas HCA Data Coordination Platform DCP (ERP123138).

# Research involving human participants, their data, or biological material

Policy information about studies with human participants or human data. See also policy information about sex, gender (identity/presentation), and sexual orientation and race, ethnicity and racism.

| | |
|---|---|
| Reporting on sex and gender | Patient sex reported in Table 1 is based on information contained in each patient's electronic medical record. Sex was not used to determine inclusion in the study. Sex based analyses are not included because 10 of 11 patients are female, consistent with the prevalence of SLE. |
| Reporting on race, ethnicity, or other socially relevant groupings | Information on race, ethnicity, or other social groupings was not included in our data or analysis. |
| Population characteristics | Population characteristics are included in Table 1. |
| Recruitment | Patients were recruited either during hospital admission at New York Presbyterian Hospital / Columbia University Irving Medical Center for cardiac symptoms or during routine follow up care at the Columbia University Lupus Center. To reduce bias, patients were recruited without any prior knowledge of their level of myocardial inflammation. |
| Ethics oversight | Columbia University Institutional Review Board |

Note that full information on the approval of the study protocol must also be provided in the manuscript.

# Field-specific reporting

Please select the one below that is the best fit for your research. If you are not sure, read the appropriate sections before making your selection.

☒ Life sciences  ☐ Behavioural & social sciences  ☐ Ecological, evolutionary & environmental sciences

For a reference copy of the document with all sections, see nature.com/documents/nr-reporting-summary-flat.pdf

# Life sciences study design

All studies must disclose on these points even when the disclosure is negative.

| | |
|---|---|
| Sample size | Our full cohort included n=3 healthy controls, n=3 Myo- patients, n=4 Myo+SD- patients and n=4 Myo+SD+ patients. The sample sizes for patient groups were based on the relative availability of serum samples. 4-6 engineered tissues, or 3-6 wells were used for each patient autoantibody sample to allow determination of statistical significance while maintaining a feasible experimental scale. |
| Data exclusions | Engineered tissues were excluded from analysis if they did not pass quality control (successful capturing at 1Hz stimulation during baseline measurements). Outliers in tissue function were excluded if outside the ±1.5 the interquartile range, as described in the methods. For other assays, Tukey's test for outlier exclusion was utilized with GraphPad Prism 10.0. For Ki67 anlaysis, image fields with >200 or <95 cells were excluded from analysis. |
| Replication | All data were reproducible, and successfully replicated. All replicates for each type of experiment are indicated in the manuscript. A minimum of three biological replicates were used for most experiments. |
| Randomization | Bioreactors containing engineered cardiac tissues were randomly allocated between different experimental groups. Tissues within the same bioreactor (up to six) were all assigned to the same group. |
| Blinding | The investigators responsible for acquiring data were blinded to the experimental groups. Data analysis was also performed blinded whenever possible. |

# Reporting for specific materials, systems and methods

We require information from authors about some types of materials, experimental systems and methods used in many studies. Here, indicate whether each material, system or method listed is relevant to your study. If you are not sure if a list item applies to your research, read the appropriate section before selecting a response.

## Materials & experimental systems

| n/a | Involved in the study |
|---|---|
| ☐ | ☒ Antibodies |
| ☐ | ☒ Eukaryotic cell lines |
| ☒ | ☐ Palaeontology and archaeology |
| ☒ | ☐ Animals and other organisms |
| ☒ | ☐ Clinical data |
| ☒ | ☐ Dual use research of concern |
| ☒ | ☐ Plants |

## Methods

| n/a | Involved in the study |
|---|---|
| ☒ | ☐ ChIP-seq |
| ☐ | ☒ Flow cytometry |
| ☒ | ☐ MRI-based neuroimaging |

## Antibodies

| Antibodies used | Anti-alpha-actinin: Sigma-Aldrich #A7811, Clone EA-53, Lot #0000111492, 1:750.<br>Anti-vimentin: Abcam #ab24525, Lot #GR3354892-4, 1:2500<br>Anti-ki67: Abcam, cat. no. ab15580, Lot #GR309524-1, 1:100<br>Secondary Goat Anti-Chicken IgY (H+L) Alexa Fluor 488 Conjugate, Thermo Fisher # A-11039, Lot #2566343, 1:1000<br>Secondary Goat Anti-Chicken IgY (H+L) Alexa Fluor 568 conjugate. Thermo Fisher #A11041, Lot #1383072, 1:1000<br>Secondary Donkey Anti-Rabbit IgG (H+L) Alexa Fluor 488 Conjugate: Thermo Fisher #A21206, Lot #2156521, 1:1000<br>Secondary Donkey Anti-Mouse IgG (H+L) Alexa Fluor 647 Conjugate: Thermo Fisher #A31571, Lot #1984047, 1:1000<br>Secondary Goat Anti-Mouse IgG (H+L) Alexa Fluor 546 conjugate: Thermo Fisher #A11030, Lot # 2465085, 1:500<br>Secondary Goat anti-Human IgG Fc , 568 conjugate:  Thermo Fisher #A21090, Lot # 1316679, 1:500<br>Secondary Goat Anti-Human IgG (H+L), 647 conjugate, Sigma Aldrich, #SAB4600181, Lot # 21C1008, 1:500 |
|---|---|
| Validation | All antibodies were validated for the applications in this manuscript by the reported manufacturer and the information is located in their website. |

## Eukaryotic cell lines

Policy information about cell lines and Sex and Gender in Research

| Cell line source(s) | The WTC11-GCaMP6f iPSC line was provided by Dr. Bruce Conklin at the Gladstone Institutes through a material transfer agreement.<br>Primary human ventricular cardiac fibroblasts (NHCF-V; Lonza, cat. no. CC-2904)<br>Human peripheral blood mononuclear cells (Stem Cell Technologies, cat. no. 70025.2) |
|---|---|
| Authentication | Pluripotency was verified by  staining for OCT4, NANOG, and SOX2; GCaMP activity was confirmed by fluorescent imaging. |
| Mycoplasma contamination | All cell lines tested negative for mycoplasma contamination. |
| Commonly misidentified lines (See ICLAC register) | No commonly misidentifed cell lines were used in this study according to ICLAC register of misidentified cell lines. |

## Plants

| Seed stocks | *Report on the source of all seed stocks or other plant material used. If applicable, state the seed stock centre and catalogue number. If plant specimens were collected from the field, describe the collection location, date and sampling procedures.* |
|---|---|
| Novel plant genotypes | *Describe the methods by which all novel plant genotypes were produced. This includes those generated by transgenic approaches, gene editing, chemical/radiation-based mutagenesis and hybridization. For transgenic lines, describe the transformation method, the number of independent lines analyzed and the generation upon which experiments were performed. For gene-edited lines, describe the editor used, the endogenous sequence targeted for editing, the targeting guide RNA sequence (if applicable) and how the editor was applied.* |
| Authentication | *Describe any authentication procedures for each seed stock used or novel genotype generated. Describe any experiments used to assess the effect of a mutation and, where applicable, how potential secondary effects (e.g. second site T-DNA insertions, mosiacism, off-target gene editing) were examined.* |

# Flow Cytometry

## Plots

Confirm that:

☒ The axis labels state the marker and fluorochrome used (e.g. CD4-FITC).

☒ The axis scales are clearly visible. Include numbers along axes only for bottom left plot of group (a 'group' is an analysis of identical markers).

☒ All plots are contour plots with outliers or pseudocolor plots.

☒ A numerical value for number of cells or percentage (with statistics) is provided.

## Methodology

| | |
|---|---|
| Sample preparation | iPSC-derived cardiomyocytes were differentiated and dissociated, followed by staining with patient IgG samples, CF-647 conjugated anti-human IgG as described in the method section. In addition, hiPSC-CMs and PBMCS were stained with MitoTracker Green, TMRM and propidium iodide. |
| Instrument | Bio-Rad ZE5 Cell Analyzer |
| Software | Bio-Rad Everest Software was used to collect data, and FlowJo 10.10 was used for data analysis. |
| Cell population abundance | All MFI values reported are based on gated populations with a frequency > 0.57% of the total events. |
| Gating strategy | The gating strategy is provided in Extended Data Figure 3e-h, 7b-d, and 8e-g |

☒ Tick this box to confirm that a figure exemplifying the gating strategy is provided in the Supplementary Information.